Peer reviewed version

## University of Bristol - Explore Bristol Research
### General rights

# Explicit Expression of Weighting Factor for Improved Estimation of Numerical Flux in Local-inertial Models

**B. Sridharan[1], Dinakar Gurivindapalli[2], Soumendra Nath Kuiry[3,*],Vijay Kisan Mali[4], N. Nithila Devi[5], Paul D. Bates[6], and Dhrubajyoti Sen[7]**

[1,4,5]Research Scholars, Hydraulics and Water Resources Engineering Division, Department of Civil Engineering, IIT Madras, India

[2]Master student, Hydraulics and Water Resources Engineering Division, Department of Civil Engineering, IIT Madras, India

[3]Assistant Professor, Hydraulics and Water Resources Engineering Division, Department of Civil Engineering, IIT Madras, India

[6]Professor, School of Geographical Sciences, University of Bristol, University Road, Bristol BS8 1SS, UK

[7]Professor, Department of Civil Engineering, IIT Kharagpur, India

[*]Corresponding author: Soumendra Nath Kuiry (snkuiry@iitm.ac.in)

**Key Points:**

- The inertial formulation of the St. Venant equations is unstable when applied to low friction areas typical of urban environments.

- Numerical stability is improved using the diffusive term but calibration is required to obtain an optimal value of the diffusion coefficient.

- This study proposes an explicit expression for the diffusion coefficient, obviating the need for trial and error calibration.

**Abstract**

Two-dimensional shallow water models have been widely used in forecasting, risk assessment and management of floods. Application of these models to large-scale floods with high-resolution terrain data significantly increases the computation cost. In order to reduce computation time, shallow water models are simplified by neglecting the inertial and/or convective acceleration terms in the momentum equations. The local-inertial models have proved to significantly improve the computational efficiency even for large scale flood forecasting. However, instability issues are encountered on smooth surfaces of urban areas having low friction values. This problem was resolved by de Almeida et al. (Water Resources Research 48: 1 - 14, 2012) by introducing limited artificial diffusion in the form of weighting factors for the neighboring fluxes. The arbitrary value of the weighting factor poses a practical limitation of being case specific and requiring calibration for accurate solutions. This study derives an explicit expression for the weighting factor, an adaptive formulation dependent on local velocity, flow depth, grid and time step size, that eliminates the need for trials and approximations. Comparisons between analytical, experimental and real-world applications confirm the accuracy and robustness of the proposed weighting factor. Implementation of adaptive weights results in less computation time compared to LISFLOOD-FP (~1.2 times) and hold a significant advantage over HEC-RAS (~25.9 times) as it allows the use of larger time step at higher CFL values. The contribution of the present study therefore resolves an important problem of current large scale flood simulations, especially those implemented in real-time.

**Keywords:** Flood modeling; Local-inertial model; Adaptive weighting factor; Chennai flood 2015

## 1 Introduction

Flood inundation is considered as a major natural hazard. Its accurate prediction is therefore necessary for developing flood hazard zone maps and issuing warnings before the occurrence of extreme flood events. Mathematical models simulating the physics thus play a pivotal role in these flood risk assessment tools. Most models solve the depth-averaged two-dimensional (2D) shallow water equations (SWEs) and in the past few decades, substantial research has gone into the development of various numerical schemes that form the basis of these models (Peraire et al., 1986; Bermudez et al., 1991; Hubbard, 1999; Sanders et al., 2008; Liang, 2010; Cea and Blade, 2015). In spite of the high-computational power and substantial progress in numerical methods, application of these models to large-domain with high-resolution topographical details, especially for issuing early warnings, demands high computation time (de Almeida et al., 2012). Simulation at high-resolution is particularly important in urban areas for capturing the complex hydrodynamic processes with a detailed representation of topographical features (Horritt and Bates, 2001; Brown et al., 2007; Fewtrell et al., 2008; Neal et al., 2009; Horritt et al., 2010; Sampson et al., 2012). This indicates the limitations of using complete 2D models for simulating floods over large areas at high resolution. In order to reduce the computational burden, four different speed-up approaches are currently employed: (i) high-performance parallelization approach that takes advantage of general purpose graphics processing unit (GPGPU) (Kalyanapu et al., 2011), distributed memory parallelization (Pau and Sanders, 2006, Neal et al., 2009), multi-core central processing units (MCs), cloud computing (Lamb et al., 2009), etc.; (ii) a simplified hydraulic model approach, in which one (i.e. convective acceleration) or both inertial terms from the complete 2D SWEs are ignored to obtain either a diffusion wave (Bates and De Roo, 2000) or a local-inertial model (de Almeida et al., 2012); (iii) a coarse-grid approach, in which the computation time is reduced either by increasing the grid size or using techniques like sub-grid treatment (Yu and Lane, 2011) and

68  porosity parameter (Sanders et al., 2008; Bruwier et al., 2017) to compensate for loss of accuracy;
69  and (iv) the Cellular Automata (CA) approach (Dottori and Todini, 2010; Guidolin et al., 2016),
70  in which the computational efficiency is improved using the universal transition rule for spatial
71  discretization. This study attempts to use the simplified hydraulic model approach, which can
72  render a much reduced computation time if implemented using techniques like GPGPU,
73  parallelization or sub-grid approach. The diffusive or local-inertial models adopt simpler
74  numerical methods for its solution algorithm. As a result, the computational cost of simplified
75  models for each time step is significantly reduced in comparison to the equivalent numerical
76  solution of full 2D models (Bates et al., 2010; de Almeida et al., 2012; Shustikova et al., 2019).
77  This improvement in computational efficiency has allowed the use of simplified models to a new
78  range of applications, such as Monte Carlo simulations for estimating uncertainty (Aronica et al.,
79  2002) and ensemble simulations for flood forecasting (Pappenberger et al., 2005).

80  Of the two simplified SWE formulations that have been developed, the local-inertial formulation
81  provides a better alternative to the diffusive wave approximation. The main advantage of the local-
82  inertial formulation lies in the improved stability condition that can be used to determine the time
83  step. The time step for the local-inertial model reduces linearly with grid size, unlike diffusive
84  wave models where the time step decreases quadratically (Bates et al., 2010). This is because the
85  local-inertial formulation is a shallow water model and the time step is therefore controlled by the
86  Courant-Friedrichs-Lewy (CFL) condition, rather than the more restrictive time step constraint
87  necessary for the diffusion wave equation developed by Hunter et al. (2005). This property of
88  local-inertial models thus substantially enhances the computational efficiency even for problems
89  with fine grids that would have been prohibitively expensive to be solved with diffusive models.
90  Also, it avoids the dramatic reduction in time step that is usually the case for diffusive wave models
91  in regions of negligible water surface gradient. Several local-inertial models have been developed
92  based on different numerical schemes (Ponce, 1990; Xia, 1994; Aronica et al., 1998; Bates et al.,
93  2010; Martins et al., 2015). Among these, the scheme proposed by Bates et al. (2010) for solving
94  the local-inertial equations is widely used for its relative simplicity and low computation cost.
95  Recent versions of the local-inertial model, LISFLOOD-FP, are based on the numerical solution
96  scheme given by Bates et al. (2010). This scheme has been successfully used for flood inundation
97  modeling in various parts of the world such as Europe (Bates et al., 2010), West Africa (Neal et
98  al., 2012), the Amazon (Baugh et al., 2013), India (Sanyal et al., 2013; Lewis et al., 2013) and
99  North Africa (Yan et al., 2014). The European Flood Awareness System (https://www.efas.eu/)
100 uses LISFLOOD-FP as its hydraulic model for the flood forecasting of entire Europe. The
101 landscape evaluation model CAESAR-LISFLOOD (Coulthard et al., 2013) uses the local-inertial
102 formulation of Bates et al. (2010) for its hydraulic simulation. MGB-IPH is another model that
103 uses the same solution scheme of Bates et al. (2010) for flow routing and has been applied for
104 large-scale flood simulations (de Paiva et al., 2013, Pontes et al., 2017). CaMa-Flood, which is a
105 global river model, developed by Yamazaki et al. (2013) also uses the local-inertial formulation.
106 These local-inertial models run on the scheme proposed by Bates et al. (2010) and are shown to
107 outperform both diffusive as well as full 2D models in terms of computational efficiency for sub-
108 critical flows (Neal et al., 2012; de Almeida et al., 2013).

109 Despite its high performance, the solution scheme was reported to suffer from numerical instability
110 under certain flow conditions in low friction regions such as urban areas (Bates et al., 2010). In
111 order to overcome this issue, de Almeida et al. (2012) proposed an improvement by introducing
112 an artificial diffusive term for accurate estimation of the numerical flux. The numerical diffusion

is added to the flux computed through an interface of a computational cell using the discharge values of the neighboring interfaces. The amount of diffusion is limited and controlled by a weighting factor $(\theta)$ which is effectively a diffusion coefficient (de Almeida et al., 2012). Two numerical schemes (q-schemes), namely, upwind and centered schemes were proposed by de Almeida et al. (2012) based on the way the weight is applied to the flux calculations. These schemes were shown to provide smooth solutions even for a wide range of friction values (down to values of Manning's friction coefficient ($n$) of 0.01 $m^{-1/3}$s), unlike the numerical solution of Bates et al. (2010) which had a tendency to break down for values of $n < 0.03$ $m^{-1/3}$s. However, the accuracy of the solution depends on the value of the parameter $\theta$, which is chosen empirically. It is observed from the applications of the LISFLOOD-FP model that stable solutions are obtained for the range $0.7 < \theta < 1.0$. Since the value of $\theta$ controls the amount of diffusion, that is the flux, its value needs to be optimized through trial and error. Martins et al. (2015) have argued that this poses a problem since the calibration procedure makes use of real-world data for obtaining the best value of $\theta$. To overcome this issue, they proposed a well-balanced local-inertial model, in which the mass and momentum fluxes are computed using the Riemann solver. Although this model avoids the requirement of the trial and error procedure, it is computationally ~ 4.0 times more expensive compared to the scheme proposed in de Almeida et al. (2012) and subsequently implemented in LISFLOOD-FP. This motivates formulating an explicit expression for $\theta$ to be used in local-inertial models such as LISFLOOD-FP. Such an expression is derived in this paper based on the local flow dynamics at each computational cell boundary and eliminates the need for the trial and error approximation of $\theta$. Considering the range of applications an explicit expression for estimating the value of $\theta$ is expected to improve the accuracy and numerical stability of LISFLOOD-FP model.

This study, therefore, aims at formulating an expression for $\theta$ to automatically control the amount of diffusion for calculating flux in the solution scheme of de Almeida et al. (2012). The value of $\theta$ varies both spatially and temporally, adapting itself automatically with those of the local variables. The adaptive expression for $\theta$ is then implemented into the upwind and centered schemes, also termed as s-schemes, of the local-inertial formulations as described in de Almeida et al. (2012). The accuracy is first verified by solving a 1D analytical test case. The 2D flood flows observed in an experimental river-network-floodplain setup is simulated to demonstrate the effect of $\theta$ on the performance of s-schemes and the LISFLOOD-FP model. Then a real-time urban flood event in Glasgow, UK, is simulated to show the improved stability condition of adaptive $\theta$ based s-schemes compared to the use of constant $\theta$ in q-scheme of de Almeida et al. (2012). Finally, s-schemes are applied to one of the most devastating floods in the history of Chennai city in Southern India that occurred in 2015. It is observed that the proposed adaptive $\theta$ for local-inertial model not only automatically controls the amount of diffusion but also increases the computational time step size as and when required. As a result, a significant reduction in computation time is also achieved in the reported applications compared to LISFLOOD-FP. The detailed analyses and comparisons of results imply that the contribution of this study in formulating an explicit expression for adaptive $\theta$ improves accuracy, computational efficiency and stability of a local-inertial model.

## 2 Governing Equations

The governing equations for the proposed model are derived by simplifying the 2D SWEs. The simplification is primarily based on the assumption that for slowly varying flows the convective acceleration terms can be neglected (de Almeida et al., 2012) and the resulting system of local-inertial equations can be written as

$$\frac{\partial h}{\partial t} + \frac{\partial q_x}{\partial x} + \frac{\partial q_y}{\partial y} = 0 \tag{1}$$

$$\frac{\partial q_x}{\partial t} + gh\frac{\partial H}{\partial x} + \frac{gn^2 |q_x| q_x}{h^{7/3}} = 0 \tag{2}$$

$$\frac{\partial q_y}{\partial t} + gh\frac{\partial H}{\partial y} + \frac{gn^2 |q_y| q_y}{h^{7/3}} = 0 \tag{3}$$

where $t$ is the time; $x$ and $y$ are the Cartesian directions; $h$ is the water depth, $q_x$ and $q_y$ are the unit width discharges in the $x$- and $y$-directions, respectively; $H = h + z$ is the water surface elevation; $z$ is the bed elevation with respect to a datum and $g$ is the acceleration due to gravity. The numerical scheme adopted herein uses the simplified momentum equations (2) and (3) in the two spatial directions for updating corresponding unit discharges, which in turn are used to compute mass fluxes in equation (1). In the next step, equation (1) is used to update the unknown water surface elevation at the cell centroid. The numerical discretization of the above governing equations is discussed in the following section.

## 3 Numerical scheme

The computational domain is described by a structured grid (Figure 1) which has the advantage to exploit the expanding wealth of raster terrain data. The mass and simplified inertial momentum equations are discretized using the Godunov like approach, in which the mass fluxes are computed through the interfaces ($i \pm 1/2$ and $j \pm 1/2$) of a cell using a simple analytical equation and the water depth is updated at the cell center $(i, j)$ (de Almeida et al., 2012).

Equation (1) is discretized for a computational cell as shown in Figure 1 using a first-order forward time marching scheme as follows

$$\frac{h_{i,j}^{t+\Delta t} - h_{i,j}^{t}}{\Delta t} = \frac{q_{i-1/2,j}^{t+\Delta t} - q_{i+1/2,j}^{t+\Delta t}}{\Delta x} + \frac{q_{i,j-1/2}^{t+\Delta t} - q_{i,j+1/2}^{t+\Delta t}}{\Delta y} \tag{4}$$

where $\Delta x$ and $\Delta y$ are the cell sizes in the $x$-and $y$-directions, respectively; $\Delta t$ is the time step size; $h_{i,j}^{t}$ and $h_{i,j}^{t+\Delta t}$ are the water depths at the cell centroid in the current and next time steps respectively; $q_{i+1/2,j}^{t+\Delta t}$ and $q_{i-1/2,j}^{t+\Delta t}$ are the mass fluxes through the interfaces ($i\pm1/2$, $j$) along the $x$-direction; and $q_{i,j+1/2}^{t+\Delta t}$ and $q_{i,j-1/2}^{t+\Delta t}$ are the mass fluxes through the interfaces ($i$, $j\pm1/2$) along the $y$-direction. The mass flux $q^{t+\Delta t}$ at an interface is computed after solving the corresponding momentum equation.

5

183 The local-inertial momentum equations (2) and (3) are also similarly discretized, for example, the
184 flux along the *x*-direction at the interface ($i-1/2, j$) is written using equation (2) as

185
$$\frac{q_{i-1/2,j}^{t+\Delta t} - q_{i-1/2,j}^{t}}{\Delta t} + g h_{flow} S_t + \frac{g n^2 \left| q_{i-1/2,j}^{t} \right| q_{i-1/2,j}^{t}}{h_{flow}^{7/3}} = 0 \tag{5}$$

186 where, $S_t = \partial H / \partial x$ is the water surface gradient and $h_{flow}$ represents the effective flow depth across
187 the interface (*i*-1/2, *j*). The effective flow depth at an interface is estimated as
188 $h_{flow} = \max(H_{i,j} - H_{i-1,j}) - \max(z_{i,j} - z_{i-1,j})$. Hence, equation (5) may now be used to explicitly
189 compute $q^{t+\Delta t}$ at an interface using the known values of $q^t$, $h^t$ and $z$. A further improvement may
190 also be made in equation (5) by replacing one $q^t$ in the friction term by $q^{t+\Delta t}$, as instabilities may
191 still arise at shallow depths (e.g. near the wet-dry interface), where the friction term becomes too
192 large (Bates et al., 2010; Kuiry et al., 2010). This substitution leads to an explicit equation for the
193 unknown $q_{i-1/2,j}^{t+\Delta t}$ with improved convergence properties similar to that of an implicit time stepping
194 scheme. Rearranging terms, equation (5) reads as under:

195
$$q_{i-1/2,j}^{t+\Delta t} = \frac{q_{i-1/2,j}^{t} - g h_{flow} \Delta t S_t}{\left( 1 + g n^2 \Delta t \left| q_{i-1/2,j}^{t} \right| / h_{flow}^{7/3} \right)} \tag{6}$$

196 Equation (6) is used to compute mass fluxes through the interface, ($i-1/2, j$). Similarly, fluxes
197 through the other three interfaces of the cell ($i, j$) can be obtained by following the above
198 discretization procedure. Once the fluxes are computed, equation (4) is used to explicitly update
199 the unknown flow depth at the center of a cell, $h_{i,j}^{t+\Delta t}$. The solution methodology followed here is
200 similar to the semi-implicit scheme proposed by Bates et al. (2010). Equation (6) improves the
201 computational efficiency significantly due to the fact that the time step is computed using the CFL
202 condition instead of the more restrictive time step constraint proposed by Hunter et al. (2005).
203 However, the finite difference technique of discretizing the spatial derivatives leads to lack of
204 diffusive terms. As a result, the scheme suffers from numerical instability at low friction values (*n*
205 < ~0.03) as the dampening effect reduces. de Almeida et al. (2012) conducted a detailed study for
206 counteracting the instabilities by incorporating a diffusion like term in equation (6). The diffusion
207 term is in fact a modification of $q_{i-1/2,j}^{t}$ in the numerator of equation (6) by taking the contribution
208 of fluxes from the neighboring cells. In effect, such a modification improves the estimation of
209 fluxes through a cell boundary by considering a larger stencil in a similar way to that of upwind
210 and centered schemes. However, this simple modification in equation (6) has been shown to yield
211 a large improvement in the numerical stability of the local-inertial models (de Almeida et al., 2012)
212 at low friction values.

213 **3.1 Numerical schemes with diffusive terms**

214 de Almeida et al. (2012) proposed two schemes (i.e. q-schemes), termed as (a) q-upwind and (b)
215 q-centered, depending on the way the information from the neighboring cell(s) is used to introduce
216 the dissipation effect. For example, in case of the q-upwind scheme, flux at the interface
217 ($i-1/2, j$) - $q_{i-1/2,j}^{t+\Delta t}$, is obtained by adding a small amount of flux from either the left or right of

6

218 its neighboring interfaces based on the direction of flow. The modified flux equation at an interface
219 is thus computed as

220
$$q_{i-1/2,j}^{t+\Delta t} = \begin{cases} \dfrac{\theta q_{i-1/2,j}^{t} + (1-\theta) q_{i-3/2,j}^{t} - g h_{flow} \Delta t S_{t}}{\left(1 + g n^2 \Delta t \left| q_{i-1/2,j}^{t} \right| / h_{flow}^{7/3}\right)} & \text{if } q_{i-1/2,j}^{t} > 0 \\[4mm] \dfrac{\theta q_{i-1/2,j}^{t} + (1-\theta) q_{i+1/2,j}^{t} - g h_{flow} \Delta t S_{t}}{\left(1 + g n^2 \Delta t \left| q_{i-1/2,j}^{t} \right| / h_{flow}^{7/3}\right)} & \text{if } q_{i-1/2,j}^{t} < 0 \end{cases}$$
(7)

221

222 For the q-centered scheme, the weighting of fluxes from both neighboring interfaces is used to
223 stabilize the solution. The flux $q_{i-1/2,j}^{t+\Delta t}$, for example, is computed as

224
$$q_{i-1/2,j}^{t+\Delta t} = \frac{\theta q_{i-1/2,j}^{t} + (1-\theta)\left(\dfrac{q_{i-3/2,j}^{t} + q_{i+1/2,j}^{t}}{2}\right) - g h_{flow} \Delta t S_{t}}{\left(1 + g n^2 \Delta t \left| q_{i-1/2,j}^{t} \right| / h_{flow}^{7/3}\right)}$$
(8)

225 In equations (7) and (8), $\theta$ is the empirical flux weighting factor. The terms associated with (1- $\theta$)
226 in the same equations are called the diffusive terms. The value of $\theta$ controls the amount of
227 dissipation and gives non-oscillatory water surface profile when an appropriate value for $\theta$ is
228 chosen. With $\theta = 1$, the semi-implicit scheme of Bates et al. (2010) is obtained, which is found to
229 give numerical instability for $n < 0.03$ m$^{-1/3}$s (de Almeida et al., 2012). $\theta = 0$ results in a scheme
230 similar to the Lax diffusive. de Almeida et al. (2012) used a constant value for $\theta$ (such as, 0.8 and
231 0.9) to improve the stability for the test cases in their study. However, this constant value needs to
232 be fixed for each case through a trial process. The derivation of the proposed closed-form solution
233 for $\theta$, which being based on the local flow characteristics obviates the need for its ad hoc selection,
234 is presented in the following section.

235 **3.2 Expression for adaptive theta**

236 The terms of q-schemes given by equations (7) and (8) are inspired by the concept of upwinding
237 and centered schemes, respectively (de Almeida et al., 2012). These equations mainly use the
238 direction of flow (i.e., towards left or right along *x*-direction and towards top or bottom along *y*-
239 direction) to obtain the artificial diffusive terms but neglect the directions of individual waves, as
240 in the case of the full SWEs. Hence, considering the similarities with upwind and centered schemes
241 (de Almeida et al., 2012), the same names are used in this study. However, it is important to note
242 that the inclusion of the diffusive terms in equations (7) and (8) is akin to the concept of the
243 weighted average flux (WAF) method (Toro, 2001). Ying et al. (2004) used a similar concept of
244 applying weights computed from the CFL number as a function of velocity, time step and grid
245 size, to remove oscillations associated with the centered discretization of the bed slope terms.
246 Following the concept of Ying et al. (2004), a simple expression as given below, is proposed here
247 for computing the weighting factor.

248
$$\theta_{i-1/2,j} = 1 - c_{i-1/2,j}^{r}$$
(9)

249 and

7

250
$$c^r_{i-1/2,j} = \frac{\Delta t}{\Delta x} u_{i-1/2,j} \qquad (10)$$

251    where $c^r_{i-1/2,j}$ is the interface CFL number.

252    The CFL number is generally used as the criteria for stability in shallow water models and the
253    minimum value of CFL within a time step is obtained by a heuristic search through all the cells of
254    the computational domain. However, implementation of a minimum value of CFL and
255    subsequently a single value of $\theta$ at all cell interfaces is found to under/over predict the solution,
256    as in de Almeida et al. (2012). One possible reason could be that the flux at all the interfaces cannot
257    be scaled by a single value of $\theta$ as it may not consider the effect of local flow dynamics. Therefore,
258    it is proposed to compute $\theta$ at all the interfaces at each time step considering the local flow velocity
259    and water depth for better accuracy. Since local-inertial models do not compute velocity as a
260    solution variable, the velocity at a typical interface, for example $u_{i-1/2,j}$ (Figure 1) is obtained from
261    the calculated discharge value as,

262
$$u_{i-1/2,j} = \frac{\left| q_{i-1/2,j} \right|}{h_{flow}} \qquad (11)$$

263    The expression of the diffusion coefficient thus becomes

264
$$\theta_{i-1/2,j} = 1 - \frac{\Delta t}{\Delta x} u_{i-1/2,j} \qquad (12)$$

265    It is found that near the wet-dry interface, $\theta$ may become very small or even negative as the second
266    term on the right side of equation (9) may turn out to be greater than unity. For that reason, the
267    wave celerity at the interface is also considered and the expression for $\theta$ is redefined as

268
$$\theta_{i-1/2,j} = 1 - \frac{\Delta t}{\Delta x} \min \left( u_{i-1/2,j}, \sqrt{gh_{flow}} \right) \qquad (13)$$

269    It can be observed from equation (13), that more diffusion from the neighboring interface is
270    introduced when the flow velocity is high, while it tends to be zero in the region having negligible
271    water surface slope. Since this weighting factor is likely to change both spatially and temporally
272    depending upon the value of discharge and water depth, it may be referred to as "*adaptive*
273    *weighting factor*" or simply "*adaptive θ*". The proposed expression for $\theta$ as given in equation (13)
274    is substituted in equations (7) and (8) and the modified form of q-schemes (q-centered and q-
275    upwind) are re-named as s-schemes (s-upwind and s-centered) in this study. Though the proposed
276    s-schemes involve a few extra computations compared to q-schemes, the numerical experiments
277    presented subsequently prove that improved numerical stability achieved at higher CFL numbers
278    to compensate the additional computational cost. Martins et al. (2015) also neglected the
279    convective acceleration term aiming to reduce the computation time of a full 2D model by applying
280    a well-balanced Roe scheme for computing mass and momentum fluxes through each cell
281    interface. Following this, the momentum and water depth at the cell centroids are updated.
282    However, the present implementation of the same scheme proves that the use of the shock-
283    capturing algorithm of Roe results in more than twice the computation time compared to the local-

8

inertial schemes. This is quite obvious since local-inertial models do not solve the mass and momentum equations separately and the Roe scheme based finite volume solution is restricted by CFL number (Kuiry et al., 2008). Therefore, the proposed adaptive $\theta$ has the potential to improve the numerical stability of local-inertial models and also to reduce the overall computation time.

## 4 Stability condition

The model time step is evaluated as suggested in Bates et al. (2010)

$$\Delta t = \alpha \frac{\Delta x}{\sqrt{gh_{\text{max}}}} \tag{14}$$

where $h_{\text{max}}$ is the maximum depth at any time step and $\alpha$ is the CFL number. The s-schemes are run with $\alpha = 0.9$ for stable results and are reported herein. Both the q-schemes (de Almeida et al., 2012) have been coded in the present model since q-upwind scheme is not available in LISFLOOD-FP (version 5.8.9). The q-schemes implemented by the authors as well as the q-centered scheme in LISFLOOD-FP show numerical oscillations for $\alpha = 0.9$, hence $\alpha = 0.8$ is used for all the test cases.

## 5 Model testing and results

The performance of the proposed adaptive $\theta$ in inertial models is assessed through a variety of numerical tests as follows

$\left.\begin{array}{ll} \text{(i)} & \text{Nonbreaking wave propagation over a horizontal plane} \\ \text{(ii)} & \text{Nonbreaking wave propagation on a planar beach} \end{array}\right\}$ Analytical tests

$\text{(iii)}$ Steady flood flow in a river-network-floodplain setup$\Big\}$ Experimental tests

$\left.\begin{array}{ll} \text{(iv)} & \text{An urban flood event in Glasgow, UK} \\ \text{(v)} & \text{Chennai (India) flood of 2015} \end{array}\right\}$ Applications

The results of the s-schemes are compared with those obtained from analytical solutions, LISFLOOD-FP (de Almeida et al., 2012), full dynamic version of HEC-RAS 2D (Brunner, 2016), TELEMAC 2D (Hervouet, 2000) and the results reported in Hunter et al. (2008).

## 5.1 Non-breaking wave propagation on a horizontal plane

This case is simulated here to assess the sensitivity of $\theta$ in q-schemes and the proposed adaptive $\theta$ in s-schemes on overall accuracy when Manning's roughness is varied from smooth surface to a numerically challenging low value. Hunter et al. (2005) developed an analytical solution for this problem by simplifying the full Saint-Venant equations, where water depth is expressed as a function of space and time as given below.

$$h(x,t) = \left[\frac{7}{3}\left(C - n^2 u^3 (x - ut)\right)\right]^{3/7} \tag{15}$$

9

313    where $u$ is the constant velocity along the $x$-direction, $n$ is the Manning's roughness coefficient,
314    and $C$ is an integration constant which can be obtained using $h(u,t)=0$. The upstream boundary
315    condition of time-varying depth is imposed at $x=0$ as

316    $$h(0,t)=\left(\frac{7}{3}n^2u^3t\right)^{3/7}$$    (16)

317    The computation domain consists of $32 \times 240$ square cells each of size 25 m $\times$ 25 m. The upstream
318    boundary condition is imposed along the entire width of the domain and as a result the problem
319    reduces to 1D wave propagation along the $x$-direction. Two simulations are performed with
320    different Manning's coefficients, $n = 0.01$ and $0.005$ m$^{-1/3}$s, with upstream velocities, $u = 0.4$ and
321    $0.635$ m/s respectively. These velocities and roughness coefficients are chosen to maintain the
322    same boundary condition as given by equation (16). The friction value of $0.01$ m$^{-1/3}$s is chosen to
323    represent smooth surfaces (e.g., the cemented surface in urban areas) and the very low friction of
324    $0.005$ m$^{-1/3}$s is chosen to investigate the ability of the proposed schemes in providing oscillation-
325    free solutions under a numerically challenging condition. The simulations are run for a duration of
326    9000 s. Since q-upwind scheme is not available in the recent version of LISFLOOD-FP, the q-
327    schemes implemented by authors and the analytical solutions are used here for comparison.

328    Figures 2a and 2b compare the water surface profiles of the q-schemes for $\theta = 0.8$ and 0.9 with the
329    proposed s-schemes and the analytical solutions at different instants of time. Figures 2c and 2d
330    show the magnified views of the wavefront in Figures 2a and 2b at time $t = 9000$ s. The q-centered
331    and s-centered schemes are seen to propagate the wave front with almost the same accuracy but
332    slightly slower than the corresponding analytical solutions for both the $n$ values. It is interesting to
333    note from Figures 2e and 2f that during the entire simulation period, the average adaptive $\theta$ values
334    for the s-centered scheme are 0.87 and 0.80 (Figure 2e and 2f) for $n = 0.01$ and $0.005$ m$^{-1/3}$s,
335    respectively. Also, these values are close to the fixed values of 0.90 and 0.80 for $\theta$ used by de
336    Almeida et al. (2012) in their q-centered scheme. In addition, it should be noted that the q-centered
337    scheme is almost insensitive to the value of $\theta$ within the considered range.

338    Figure 2c shows that for $\theta = 0.9$ and $n = 0.01$ m$^{-1/3}$s, the wave front propagation obtained using the
339    q-upwind scheme falls closer to the analytical solution and it is over predicted for $\theta = 0.8$.
340    However, the simulated wave front propagation by the q-upwind scheme for $n = 0.005$ m$^{-1/3}$s with
341    both the fixed values of $\theta$ are slower than the analytical solution as shown in Figure 2d. Hence, it
342    is clear that for various Manning's $n$, the q-upwind scheme is sensitive to the $\theta$ value, de Almeida
343    et al. (2012) reported that the q-upwind scheme is sensitive due to the zero-th order term and
344    dropped this scheme from the LISFLOOD-FP model. Interestingly, the s-upwind scheme
345    consistently performs better for both the $n$ values and the wave fronts are always closer to the
346    analytical solutions. This is due to the usage of adaptive $\theta$ following the local hydrodynamics such
347    as velocity as shown in Figures 2e and 2f.

348    It is also observed that the results obtained using the q-schemes fall closer to the s-schemes,
349    provided the adaptive $\theta$ value throughout the simulation period varies within a narrow range and
350    the empirically fixed $\theta$ value is chosen from that specific bound of values rather than from a wide
351    range. In this test case, though the s-upwind scheme is shown to be more accurate than the fixed

10

352 $\theta$ based q-upwind scheme, the improved accuracy of the s-centered scheme over the q-centered
353 scheme is marginal.

354 For stable results, the s-schemes and q-schemes were run with time steps of 11.68 s and 9.8 s
355 respectively. Therefore, s-schemes have been proven to be faster than q-schemes by ~1.19 times,
356 which is about ~19% improvement in overall computation time.

### 5.2 Non-breaking Wave Runup on a Sloping Beach

358 This test case proposed by Hunter et al. (2005) explores the propagation of a wave over an adverse
359 longitudinal slope. This test case examines the numerical stability of the proposed s-schemes as
360 the reduction in water depth along the adverse slope enhances the non-linear effect that in turn
361 leads to more shocks. The solution for this problem can be obtained by using a fourth order Runge-
362 Kutta method as described in de Almeida et al. (2012). The computational domain is again
363 discretized into $32 \times 240$ square cells each of size 25 m×25 m and along the longitudinal direction
364 the adverse slope of $10^{-3}$ is maintained. Two simulations are performed using the Manning's
365 coefficients, $n = 0.03$ and 0.01 $m^{-1/3}$s and the velocity of $u = 0.4$ m/s is used at the upstream for
366 both the simulations. In the absence of q-upwind scheme in the recent version of LISFLOOD-FP,
367 the q-schemes implemented by the authors and the analytical solution are used for comparisons.
368 Figures 3a and 3b show the comparisons of the simulated water surface profiles along the $x$-
369 direction with the Runge-Kutta solution at different instants of time.

370 Figures 3c and 3d show the magnified views of Figures 3a and 3b, respectively at time $t = 3600$ s.
371 For both the $n$ values, the s-schemes produce smooth solutions without any numerical oscillations
372 similar to the q-schemes as reported in de Almeida et al. (2012). The water surface profiles
373 obtained by all the centered schemes are under-predicted and the wave front propagation is slower
374 compared to the corresponding Runge-Kutta solutions. In case of the q-upwind scheme, for $\theta = 0.8$
375 , the water surface profile is over predicted and accordingly the wave front moves faster. The water
376 surface profile and wave front are closer to the Runge-Kutta solution for $\theta = 0.9$ as shown in
377 Figures 3c and 3d. On the other hand, the results of the proposed s-upwind scheme are found to be
378 consistently closer to the Runge-Kutta solutions for both the $n$ values, similar to the previous test
379 case. It can be observed that again the results from the q-schemes fall closer to those of s-schemes
380 provided the fixed value of $\theta$ (0.90 for both q-centered and q-upwind schemes) is chosen from
381 the narrow range of the adaptive $\theta$ values (average $\theta$ of 0.91 and 0.93 for q-centered and q-
382 upwind schemes, respectively) over the entire simulation period. The s-schemes are observed to
383 be ~1.15 and ~1.20 times faster than the q-schemes for $n = 0.01$ and 0.03 $m^{-1/3}$s, respectively.

384 The above two test cases prove that the proposed adaptive $\theta$ concept gives results with either
385 similar or better accuracy with less computation time compared to the q-schemes of de Almeida
386 et al. (2012) irrespective of the type of schemes and Manning's roughness values. The advantage
387 of the proposed adaptive $\theta$ concept is that the trial and error procedure required to fix $\theta$ value is
388 completely eliminated. In addition, it is found that q-upwind scheme is also consistent provided
389 that $\theta$ is chosen adaptively as provided in this study.

### 5.2 Experimental Flood Propagation in a River-Network-Floodplain Setup

391 The above test cases demonstrate the performance of the proposed s-schemes for 1D flow
392 problems. It was found that in the case of 1D flow if the fixed $\theta$ value is chosen from the narrow

11

393  range of adaptive $\theta$, the wave front computed by the q-schemes are closer to that of s-schemes. To
394  further assess the performance of s- and q-schemes for 2D flow problems, simulations are run to
395  reproduce the experimental flood event generated in a physical setup at the Hydraulics Laboratory
396  of Indian Institute of Technology Madras (IITM), India (Figure. 4). The physical model represents
397  a typical river-network-floodplain system, as commonly seen in delta regions. The setup is 20 m
398  long and 5 m wide, and consisting of 8 channels, 4 junctions and 5 distinct floodplains (F1-F5).
399  The channels are rectangular in section and are connected to the flood plains on either side. All the
400  channels slope downstream with a uniform bed slope of 1:1000. The digital topography of the
401  setup is represented by an elevation model (DEM) of 2 cm × 2 cm resolution. More details on the
402  DEM of the setup can be found in Mali and Kuiry (2018).

403  Water is released into the setup at its upstream through the main channel from an overhead tank
404  using two pipelines of diameters 8″ (203.2 mm) and 3″ (76.2 mm), respectively. The discharge of
405  water is measured using an electromagnetic flow meter. The flow rate is controlled using a sluice
406  gate in the 8″ (203.2 mm) diameter pipe and a SCADA (supervisory control and data acquisition)
407  system in the 3″ (76.2 mm) diameter pipe. The test cases are conducted for a steady-state flow of
408  0.078 and 0.098 m$^3$/s. Initially, a small amount of water at a rate of about ~0.018 m$^3$/s is released
409  into the model for one hour until initial disturbances dampen out. The inflow is then gradually
410  increased up to 0.078 and 0.098 m$^3$/s in a sufficiently long duration. The SCADA control is used
411  to avoid unnecessary wetting of the floodplains and subsequently to improve the accuracy of
412  delineated flood extent using the image processing technique. Once steady state is attained water
413  depths are measured using point gauges. The observation locations in the river (green colour) and
414  over the floodplains (light yellow colour) are shown in Figure 4. The inundation extent is captured
415  using a Nikon D5300 DSLR camera from the top. Finally, the captured images are processed in
416  ARCGIS to delineate the inundation extent. Each experiment takes about 10 hours to complete
417  and are repeated thrice to ensure the reliability of the observed water depths as well as the
418  generated inundation extent maps. The details of the experiment can be found in Mali and Kuiry
419  (2019).

420  *Calibration of Manning's n value*

421  To calibrate Manning's coefficients for LISFLOOD-FP and the proposed s-schemes the
422  simulations are conducted using the steady-state flow of 0.078 m$^3$/s. For calibration purpose,
423  Manning's coefficient is varied between 0.008-0.014 m$^{-1/3}$s for smooth concrete surface with an
424  increment of 0.001. In case of the LISFLOOD-FP model, apart from Manning's coefficients,
425  different $\theta$ values are also needed to be calibrated. The value of $\theta$ is chosen between 0.70 - 0.95
426  with an incremental step of 0.05. Hence, the LISFLOOD-FP model was run forty-two times using
427  the combinations of Manning's roughness coefficients (0.008-0.014 m$^{-1/3}$s) and weighting factors
428  (0.70 - 0.95), while the proposed s-schemes are run only for seven values of Manning's coefficient.
429  The simulations are carried out using the discharge of 0.078 m$^3$/s at the upstream and measured
430  water levels (locations shown as red dots in Figure 4) at three downstream outlets. The initial
431  condition of the model was set by specifying a uniform water depth of 0.08 m inside the river
432  network. The optimal value of Manning's coefficients for the LISFLOOD-FP and s-schemes are
433  identified by comparing the simulated inundation extents with observed maps. The simulated water
434  depth using optimal Manning's coefficients of the LISFLOOD-FP and s-schemes are then
435  compared with observed water depths to analyze their accuracy.

12

436 The accuracies of the s-schemes and the LISFLOOD-FP model in predicting the flood extent are
437 examined based on the number of wet/dry cells. For quantitative evaluation, the goodness-of-fit
438 (*F*) values are computed using the simulated and observed inundation extents. The following
439 expression used in Bates et al. (2006) and Kuiry et al. (2010) is adapted in this study to evaluate
440 the measure of fit (*F)* value as,

441
$$F = \frac{A}{A+B+C} \times 100 \quad \% \tag{17}$$

442 where *A* is the wet area correctly predicted by an inertial model, *B* and *C* are the over- and under-
443 predicted areas by a model compared to the observed data. Therefore, the value of *F* varies from
444 0 to 100 %. *F* = 0 % indicates no overlap of the predicted and observed areas and *F* = 100 %
445 indicates a perfect overlap.

446 From the simulations, it was found that the LISFLOOD-FP model significantly over-predicts the
447 inundation extent at the upstream of the flood-plain F1 when the Manning's coefficient is greater
448 than 0.009 and the value of $\theta$ is less than 0.95. The observed inundation map indicates that this
449 prediction is unphysical and apparently is caused by the use of high diffusion value (low weighting
450 factor) and Manning's coefficient. As a result of this over prediction, the accuracy of simulated
451 flood extent is reduced and *F* value is found to be less than 66%. On the other hand, the
452 LISFLOOD-FP result shows significant under-prediction of inundation extent for $\theta$ = 0.95,
453 irrespective of Manning's coefficients and the *F* values are in the range of ~56 - 68%. The realistic
454 inundation extents are simulated for Manning's coefficients of 0.008 and 0.009 m$^{-1/3}$s. Among
455 these two values, a better prediction is obtained only for Manning's coefficient of 0.009 m$^{-1/3}$s with
456 *F* = 76% (for 0.008 m$^{-1/3}$s the *F* value is 73%) when $\theta$ = 0.90. However, when $\theta$ = 0.85 these two
457 Manning's coefficients produced overprediction of inundation extents (*F* = 68% for 0.008 and
458 66% for 0.009 m$^{-1/3}$s). Hence, 0.009 m$^{-1/3}$s is treated as the calibrated value for the LISFLOOD-FP
459 model. Similarly, the calibration process is carried out for s-schemes by taking value of Manning's
460 coefficient within the range of 0.008-0.014 m$^{-1/3}$s. From the simulations, it was found that
461 Manning's coefficient of 0.01 m$^{-1/3}$s results in better prediction (*F* = 84% and 86% for s-centered
462 and s-upwind schemes, respectively) and is thus taken as the calibrated value. These calibrated
463 Manning's coefficients are then used to simulate the steady-state flow of 0.098 m$^{-1/3}$s for assessing
464 the performance of LISFLOOD-FP and s-schemes. The dependency of $\theta$ on the accuracy of the
465 LISFLOOD-FP model and the solution to this problem given by s-schemes are discussed in the
466 following sections.

467 ***Steady-sate experimental flood caused by inflow of 0.078 m³/s in a set-up***

468 To demonstrate the effect of $\theta$ on accuracies, the results of LISFLOOD-FP model obtained with
469 the calibrated *n* value of 0.009 m$^{-1/3}$s for $\theta$ = 0.85, 0.90 and 0.95 are discussed along with the
470 results of s-schemes obtained using the optimal *n* value of 0.01 m$^{-1/3}$s. The comparison of simulated
471 maximum inundation extent maps obtained from these two models are shown in Figure 5. The
472 observed inundation extent is shown in red solid line (Figure 5). For $\theta$ = 0.85, the LISFLOOD-
473 FP model produces over-prediction of the inundation extent (Figure 5a) at the upstream part of the
474 floodplain F1. The over prediction is unphysical and occurred due to the use of the constant value
475 of $\theta$. For $\theta$ = 0.9, the LISFLOOD-FP model shows better prediction as shown in Figure 5b. A
476 higher value of $\theta$ as 0.95 (Figure 5c) conversely leads to significant under-prediction of the

13

477    inundation extent. From the above three cases with various values of $\theta$, it is clear that the
478    inundation extent changes depending on the value of $\theta$ and the optimum value of $\theta$ falls between
479    0.85 and 0.90. It is therefore clear that the use of constant $\theta$ demands a trial procedure for better
480    prediction of inundation map. Figures 5d and 5e show the inundation extents predicted by s-
481    centered and s-upwind schemes, respectively. It can be observed from Figures 5d and 5e that the
482    use of adaptive $\theta$ in the s-schemes leads to the realistic prediction of the inundation extent.

483    To gain a better understanding on the effect of the value of $\theta$, the amount of diffusion at each
484    interface along the *x*-and *y*-directions are plotted along with the corresponding velocities for both
485    s-centered and s-upwind schemes (Figure 6). A comparison of the plots shows that the amounts of
486    diffusion and corresponding velocity at a location vary in a similar pattern. For instance, the
487    simulated velocity along the *x*-direction is relatively higher when compared to that along the *y*-
488    direction (Figures 6b and 6d, and Figures 6f and 6h). This velocity pattern is consistent with the
489    physical behavior as the water flows from upstream to downstream of the setup. Subsequently,
490    more diffusion is introduced by the s-schemes (Figures 6a and 6e) along the *x*-direction compared
491    to the *y*-direction (Figures 6c and 6g). On the floodplain F1, LISFLOOD-FP with $\theta$ < 0.90
492    produced unphysical over-flooding. The over-flooding is caused by a high diffusion value (~ 0.20)
493    along the *y*-direction. However, when the diffusion along the *y*-direction is less than 0.1, the
494    unphysical flooding does not occur on F1 (Figures 5d and 5e). In case of s-schemes, the proposed
495    adaptive $\theta$ automatically takes care of such variations in the diffusion based on local water depth
496    and velocity. Therefore, it produces a realistic inundation extent. The *F* values of the LISFLOOD-
497    FP and the proposed s-schemes are summarized in Table 1, from which it can be seen that the
498    proposed s-schemes show good skill in predicting inundation extents due to the use of adaptive $\theta$
499    . It may therefore be concluded that the proposed s-schemes improves the accuracy of the model
500    compared to LISFLOOD-FP.

501    In addition to inundation extent, water depths simulated using the optimal Manning's coefficient
502    (i.e., 0.009 $m^{-1/3}$s for LISFLOOD-FP and 0.01 $m^{-1/3}$s for s-schemes) is also compared with
503    observed depths in the river as well as over the floodplains. Inside the river, the LISFLOOD-FP
504    for $\theta$ = 0.90 show reasonably good agreement with the observed water depths (Figure 7) and for
505    $\theta$ = 0.85 and 0.95 the accuracy of the simulated water depths are reduced. In case of s-schemes,
506    the results agree well with the observed water depths at most of the gauges. In contrast, the
507    comparison of results from s-schemes and LISFLOOD-FP over the floodplain, show both under
508    and over prediction (Figure 8) at different gauges. However, the LISFLOOD-FP significantly over
509    and under predicts the inundation extents for $\theta$ = 0.85 and 0.95, respectively as discussed before.
510    The water depths obtained using s-schemes fall between those of the LISFLOOD-FP for $\theta$ = 0.85
511    and 0.90. The accuracy of predicted water depths estimated through the root mean square errors
512    (RMSE) are given in Table 2. From the RMSE values, it can also be confirmed that the accuracy
513    of s-schemes is better than that of the LISFLOOD-FP.

514    ***Steady-state experimental flood caused by inflow of 0.098 m³/s in a set-up***

515    The calibrated Manning's roughness values of 0.009 and 0.01 are used to further assess the
516    performance of the LISFLOOD-FP and s-schemes, for reproducing the steady-state experimental
517    flood caused by an inflow of 0.098 m³/s. The simulated inundation extents of LISFLOOD-FP for
518    $\theta$ = 0.85, 0.90 and 0.95, and the proposed s-schemes are compared with the observed map (Figure
519    9). For $\theta$ = 0.85, the LISFLOOD-FP model (Figure 9a) over predicts the inundation extent on

14

floodplains F1, F3 and F5. The over prediction is unphysical and it is because of the high diffusion value as discussed before. For $\theta = 0.90$, the predicted inundation extent is closer to the observed map (Figure 9b). In case of $\theta = 0.95$, the LISFLOOD-FP model shows under-prediction of the inundation extent (Figure 9c) at the upstream of the floodplain F1 and downstream of floodplain F2. It can be observed from Figures 9d and 9e that the s-schemes produce inundation extents closer to those observed. The accuracy of inundation extents obtained by the LISFLOOD-FP model (for $\theta = 0.85$, 0.90 and 0.95) and proposed s-schemes are compared in Table 3. The fitness values of s-schemes, once again underlines the improved predictive ability of adaptive $\theta$. To demonstrate the effect of a variation in $\theta$, the amount of diffusion along the $x$-and $y$-directions are plotted along with the corresponding velocities for both s-centered and s-upwind schemes (Figure 10). The simulated velocity along the $x$-direction is relatively higher in comparison to that along the $y$-direction (Figures 10b and 10d, and Figures 10f and 10h). Subsequently, higher diffusion is introduced by the s-schemes (Figures 10a and 10e) along the $x$-direction than in the $y$-direction (Figures 10c and 10g). On the floodplain F5, LISFLOOD-FP with $\theta = 0.85$ produces unphysical over-flooding owing to a high diffusion value (~ 0.20) along the $y$-direction. On the floodplains F1 and F4, LISFLOOD-FP with $\theta = 0.95$ under-predicts the inundation extent due to low diffusion value (~0.05) along the $y$-direction. In the case of s-schemes, adaptive $\theta$ varies the optimal amount of diffusion (~ 0.10) spatially based on local water depth and velocity (Figures 10d and 10h).This test case reconfirms the improved accuracy of s-schemes compared to LISFLOOD-FP.

Figures 11 and 12 compare the simulated and observed water depths in the river as well as over the floodplains. The results of LISFLOOD-FP show closer prediction of water depth for $\theta = 0.9$, over and under prediction for $\theta = 0.85$ and 0.95, respectively. It can be observed that water depth results from s-schemes match very well in most of the gauges inside the river. On the other hand, the simulated water depths of LISFLOOD-FP as wells as s-schemes over the floodplain are either under predicted or over predicted when compared to the observed depths. Interestingly, the water depths simulated by the s-schemes fall closer to the observed depths in most of the gauges compared to those by the LISFLOOD-FP model. The RMSE error in Table 4 suggests that the s-schemes predict water depths better than the LISFLOOD-FP model.

The relative computation time with respect to the s-centered scheme are also summarized in Tables 1 and 3, from which it can be observed that the LISFLOOD-FP model with $\theta = 0.8$ and 0.9 takes at least 18 % more computational time compared to the s-schemes. The enhanced stability condition of the proposed s-schemes allows a larger time step which in turn this improves the overall computational efficiency. The accuracy of the proposed s-schemes is shown to be consistently better than LISFLOO-FP. Therefore, it may be concluded that the proposed s-schemes will help in eliminating the trial and error process of selecting an optimal value of $\theta$ as well as improve the accuracy of predicting the inundation extent in relatively less computation time compared to LISFLOOD-FP.

**5.3 Urban flood simulation in Glasgow, UK**

This test case is simulated to demonstrate the improved stability and performance of the proposed adaptive $\theta$ for a field application in an urban environment. The area of Greenfield, a suburb of Glasgow, UK, is thus chosen as a benchmark test case for comparing the performance of 2D

15

562    numerical models for which DEM and other data is available (Hunter et al., 2008; Fewtrell et al.,
563    2008). The flooding at this site has been observed in response to a heavy rainfall event in the
564    upstream catchment. The study site consists of a densely populated urban area along two main
565    streets and topologically complex minor road networks as shown in Figure 13. The extent of the
566    rectangular domain is 970 m × 400 m.

567    On July 30, 2002, the site experienced an episode of flooding due to heavy rainfall at the upstream
568    catchment area (~ 5 km$^2$) of X0. The runoff from the upstream flows through a small stream and
569    enters the culvert at location X0 near the north-east corner (shown in Figure 13a). Beyond this
570    point, the stream runs underground throughout the entire site. The flow exceeding the carrying
571    capacity of the culvert is spilled onto the nearby surface and then flows along the two main streets
572    that are oriented in the east-west direction through points X2 and X3. After interacting with the
573    complex building network and minor road networks, the water eventually converges and ponds in
574    the low-lying area, i.e. the southern part of the domain.

575    The hydrograph reported in Hunter et al. (2008) is used to specify the inflow boundary condition.
576    The values of this hydrograph are constructed from the volume of water exceeding the carrying
577    capacity of the culvert based on the best interpretation of eyewitnesses and historical photographs.
578    For this study, such a hydrograph is digitized and imposed as the point source boundary condition
579    at X0 (Figure 13a). All external boundary conditions are closed with zero mass fluxes. Simulations
580    are carried out using the combinations of 13 friction coefficients (Table 5) chosen from physically
581    plausible range as reported in Hunter et al. (2008). To corroborate the results of the proposed s-
582    schemes, water depth results reported in Hunter et al. (2008) for two diffusive models (JFLOW
583    and LISFLOOD-FP diffusive version) and four different full 2D models (TUFLOW, DIVAST,
584    DIVAST-TVD and TRENT) are used as reference solutions. The model like JFLOW (Bradbrook
585    et al., 2004), LISFLOOD-FP (Hunter et al., 2005) use simplified versions 2D equations,
586    specifically the diffusive wave formulation, for its numerical solution. The full 2D models
587    TUFLOW (Syme, 1991) and DIVAST (Falconer, 1986) solve the SWEs by implicit schemes,
588    while DIVAST-DVT (D-TVD) (Liang et al., 2006) and TRENT (Villanueva and Wright, 2006)
589    use explicit schemes. These model results are considered as reference solutions for comparisons.
590    Two different cases are simulated for the duration of 120 minutes. In the first case, the proposed
591    s-schemes and LISFLOOD-FP (version 5.8.9) inertial model are simulated with a single set of
592    friction coefficients 0.015 m$^{-1/3}$s and 0.05 m$^{-1/3}$s as reported in Hunter et al. (2008). In the second
593    case, simulation is carried out using an ensemble of 13 friction coefficient (Table 5). These
594    identical spatially distributed friction coefficients are chosen to differentiate two land-use classes
595    such as vegetated areas and tarmac areas from the OS Mastermap$^{(R)}$ data.

596    In the first case, the time series of water depth obtained using s-schemes and LISFLOOD-FP
597    inertial model are compared at four points X1, X2, X3 and X4 (Figure 13). These representative
598    points are chosen to understand the hydraulic conditions occurring in the computational domain.
599    The excess water from the culvert at X0 moves simultaneously towards points X1 and X2. At the
600    commencement of simulation, water accumulates rapidly at point X1 as it is closer to point X0.
601    Subsequently, the accumulated water drains slowly as the simulation proceeds. It may be observed
602    from Figure 14a that the water depth predicted by s-schemes as well as LISFLOOD-FP models
603    are in good agreement with the reference solutions. Point X2 is located along one of the main
604    streets and it receives water from a single direction (from east to west). This point represents the
605    area of shallow water zone with high velocity over which the complete flood wave travels. The
606    comparison of water depths at X2 as shown in Figure 14b implies that the result from proposed s-

16

607 upwind and s-centered schemes fall closer to reference solutions. In contrast, the LISFLOOD-FP
608 inertial model produces oscillatory water depth despite using $\theta$ to remove oscillations. The
609 oscillations are more when the value of $\theta = 0.8$ or $0.9$ and are relatively less for $\theta = 0.7$. Thus the
610 results obtained for $\theta = 0.7$ (at all four stations) are reported in this section. The constant value of
611 $\theta = 0.7$, $0.8$ or $0.9$ is not able to vary the right amount diffusion required to avoid oscillations. As
612 a result, the LISFLOOD-FP inertial model becomes unstable for this combination of friction
613 coefficient and shallow water depth. Point X3 is located in the area where ponding takes place
614 eventually after receiving water from both the main streets through points X1 and X4. Therefore,
615 the water depth is relatively deep at this location than at other places. Figure 14c shows close
616 agreement of water depth simulated using the proposed s-schemes with the reference solutions,
617 whereas LISFLOOD-FP inertial model over-predicts the water depth with small numerical
618 oscillations. Point X4 represents the zone of convergent flow as it receives water along the north-
619 south direction as well. This point also experiences shallow water depth similar to point X2. The
620 water depths are compared in Figure 14d and the results by s-schemes are again observed to be
621 closer to the reference solutions. It is clear from the Figure 14 that the proposed s-schemes produce
622 smooth solutions without any numerical oscillations though with the LISFLOOD-FP inertial
623 model, such oscillations are encountered. The absolute maximum difference between the peak
624 water depths is found to be ~2 cm and ~3 cm for s-upwind and s-centered schemes, respectively.
625 The error is of the same order as the vertical error in the LiDAR DEM (RMSE of ~ 5 cm).

626 Figure 15 shows the maximum inundation extents predicted by the s-schemes and the 2D-model
627 available in LISFLOOD-FP suite. The results from the 2D-model is considered as reference
628 inundation map (Figure 20c) since there is no observed inundation map available. It can be
629 observed that s-upwind scheme behaves somewhat similar to full 2D model, while s-centered
630 scheme slightly under-predicts the extent towards the west side. Overall, inside the urban area both
631 the s-schemes produce results similar to those of the full 2D model.

632 In the second case, a mini-ensemble simulation is carried out using all the 13 pairs of roughness
633 coefficients ($n_{road}$ and $n_{veg}$) that are provided in Table 5. These identical spatially distributed
634 parameter pairs are defined based on the major classes of land-use. Parameter $n_{veg}$ is varied
635 between $0.015$ (bare earth) and $0.075$ (dense tall grass and shrubs) with the increment of $0.005$.
636 Parameter $n_{road}$ is varied between $0.008$ and $0.020$ with an interval of $0.001$. These parameter sets
637 are considered here to understand the performance of the diffusion coefficient in simulating urban
638 flood with low Manning's roughness values. The simulations are carried out for all 13
639 combinations using the LISFLOOD-FP inertial model with $\theta = 0.7$, $0.8$ and $0.9$ and s-schemes
640 with adaptive $\theta$. The best results obtained for $\theta = 0.7$ are used herein for comparative study. The
641 results of LISFLOOD-FP inertial model are compared with the maximum and minimum water
642 depths obtained from the reference solution of full 2D models (Figures 16-18). The results
643 corresponding to simulation number 1, 7 and 13 (Table 5) are discussed for clarity. The red line
644 indicates the maximum and minimum possible range of the results for different combinations of
645 Manning's coefficient (Table 5) from full 2D models. The black, blue and green lines indicate the
646 results corresponding to the simulation test sequence 1 ($n_{road}$: $0.008$, $n_{veg}$: $0.015$), 7 ($n_{road}$: $0.014$,
647 $n_{veg}$: $0.045$) and 13 ($n_{road}$: $0.020$, $n_{veg}$: $0.075$), respectively. It can be observed from Figure 21 that
648 the LISFLOOD-FP inertial model produces numerical oscillations especially at points X2 and X4.
649 For simulation number 13, the oscillations are relatively less. However, the water depths are either
650 under or over predicted. Although $\theta = 0.9$ produces smooth solutions for simulation number 13

17

651 the oscillations are more pronounced for other roughness combinations, i.e., for simulations 1 to
652 12.

653 Figures 17 and 18 show the comparison of water depths obtained using the proposed s-schemes
654 with adaptive $\theta$. It is quite clear from Figures 17 and 18 that s-schemes are able to produce smooth
655 results for all 13 combinations of the friction coefficients. The predicted water depths are found to
656 be more or less within the minimum and maximum water depths of full 2D models. The smooth
657 solutions have achieved from the use of adaptive $\theta$, which is able to vary the value of diffusion
658 $(1-\theta)$ more accurately in removing the oscillations. The relative computation time of the
659 LISFLOOD-FP model (for $\theta = 0.7$) and s-upwind scheme are 1.14 and 1.02 times more compared
660 to s-centered scheme. This case demonstrates the accuracy, robustness and the ability of adaptive
661 $\theta$ in s-schemes to produce oscillation free solutions.

662 Overall, it can therefore be concluded that the use of constant $\theta$ value based local inertial model
663 LISFLOOD-FP still suffers from numerical instability. Interestingly, the proposed s-schemes with
664 adaptive, predicts the water depth accurately and also removes the issue of numerical oscillations.

665 **5.4 Case Study on Chennai floods in 2015, India**

666 In order to investigate the applicability of the proposed adaptive $\theta$ based local-inertial model for
667 simulating large-scale floods, a rapidly urbanizing ungauged basin (Adyar) is chosen. The basin
668 comprises the Southern part of Chennai city, India. The study area, as shown in Figure 19, extends
669 between the latitudes 12°47'6" N and 13°3'22" N and longitudes 79°52'36" and E 80°17'1" E.
670 The upstream portion of the study area is dominated by shrub land and water bodies, while the
671 lower areas are a part of the Chennai Metropolitan Area (CMA). The Adyar River makes entry
672 into the city at Nandambakkam Bridge and flows through the densely populated CMA before
673 discharging into Bay of Bengal. It remains dry for most of the year but swells during the months
674 October – November, the period coinciding with North - East (NE) monsoon. The city of Chennai
675 often comes under the grip of deep depressions and cyclones during the NE monsoon. Coupled
676 with the intense precipitation during this period, the city's low-lying terrain (average elevation is
677 ~ 6 m), inefficient drainage structures, poorly maintained river and estuary hamper drainage of
678 flood waters into the sea creating recurrent massive floods. During all the flood events, the areas
679 close to Adyar River are the worst affected. Chennai and its adjacent districts experienced
680 devastating floods during November-December 2015 which caused enormous economic loss along
681 with a death toll of more than 400 people (Nithila Devi et al., 2019). The city received multiple
682 torrential rainfalls during November 8 - December 1, 2015. On December 1, extremely heavy
683 rainfall (about 60 mm/hr) was recorded that was considered to be a one in hundred year return
684 period (i.e. 0.01 annual exceedance probability) event. As a consequence of such an extreme event,
685 most parts of the city were flooded and the area adjacent to Adyar River were worst affected. The
686 applicability of the developed model can therefore be rigorously tested if such a massive flood can
687 be simulated with reasonable accuracy. For this purpose, the hydrological model HEC-HMS is set
688 up for the entire Adyar basin as shown in Figure 19, whereas the hydraulic models (inertial and
689 HEC-RAS) are set up from the confluence point (marked by a red dot in Figure 19) between the
690 canal from the Chembarambakkam reservoir and the Adyar River to the downstream boundary at
691 Bay of Bengal. The hydraulic model domain is represented by the shaded portion in Figure 19.

692 The calibration and validation of HEC-HMS for the selected flood event is presented in Nithila
693 Devi et al. (2019). The flood hydrograph obtained from HEC-HMS model at the confluence point

18

694 is applied as the inflow boundary condition to the hydraulic models. At the ocean side, the observed
695 tidal variations (Narasimhan et al., 2016) are prescribed as the downstream boundary condition.
696 The bathymetry of the river and floodplains is represented using a 10 m × 10 m resolution digital
697 elevation model (DEM). The flood event is also simulated using 2D hydraulic models HEC-RAS
698 and TELEMAC for comparison. Two 2D models results are used to examine if there is any model
699 uncertainty before considering their results as reference solutions in the absence of detailed
700 measured data for this particular event. For HEC-RAS and local-inertial models, the 150 km × 8.5
701 km model domain is discretized into square grids with cell size of 10 m × 10 m, whereas the same
702 flow domain is discretized into 59800 triangles for the TELEMAC model. It may be noted that
703 TELEMAC 2D can capture the channel alignment with high accuracy by employing unstructured
704 grids. The single Manning's $n$ values of 0.025, 0.030, 0.035, 0.040, and 0.045 $m^{-1/3}s$ as in Nithila
705 Devi et al. (2019) are used to understand the variations in the simulated results.

706 ### *Flood depth comparison*

707 For comparing the results of s-schemes, simulations are also carried out using the LISFLOOD-FP
708 model and the 2D models. All the model results are compared with high flood water marks, which
709 were surveyed soon after the flood by a team of researchers from various institutes such as IIT
710 Madras, Anna University, National Institute of Ocean Technology (Chennai), and National
711 Remote Sensing Centre (Hyderabad) using Differential Global Positioning System (DGPS) and
712 digital point gauge. The accuracy of DGPS is of the order of ± 76 mm while that of the point gauge
713 is ± 0.5 mm. It should be noted that the measured data also involves certain amount of human
714 error, which cannot be quantified (Fewtrell et al., 2011; Parkes et al., 2013). The hydraulic
715 simulations are run from November 30 to December 3, 2015. The simulated and surveyed flood
716 water-marks are compared in Figure 20. It is observed that for full 2D models, better results are
717 obtained for Manning's $n$ value of 0.035 $m^{-1/3}s$ with the RMSE error of 0.52 and 0.54 m and
718 coefficient of regression of 0.95 and 0.94 for HEC-RAS and TELEMAC models, respectively. The
719 2D models are found to maintain similar level of accuracy and hence the 2D model results can be
720 used as reference solutions, especially time-series of water depth and maximum flood extent. On
721 the other hand, s-schemes and LISFLOOD-FP are found to produce best results for Manning's $n$
722 value of 0.040 $m^{-1/3}s$. Also, LISFLOOD-FP is observed to be accurate for $\theta = 0.8$. Therefore, for
723 full 2D and inertial models Manning's $n$ values of 0.035 $m^{-1/3}s$ and 0.040 $m^{-1/3}s$ are considered as
724 the calibrated values. It can also be observed (Figure 20) that both the s-schemes are able to
725 simulate this flood event with the similar levels of accuracy, which are relatively better than
726 LISLOOD-FP model.

727 Furthermore, to assess the accuracy of the proposed s-schemes, the time-series of water depths at
728 selected locations (shown in Figure 19) are compared against LISFLOOD-FP, TELEMAC and
729 HEC-RAS results (Figure 21). The water depth profiles obtained using inertial models are found
730 to be closer to HEC-RAS results compared to TELEMAC. This might be due to the fact that the
731 inertial models and HEC-RAS use the same computational grid, in addition the solution of HEC-
732 RAS and TELEMAC models are also different. Hence, the accuracies of the local-inertial models
733 is evaluated using water depths computed by HEC-RAS as reference solutions and are enlisted in
734 Table 6 and 7. It can be observed from Table 6 that the proposed s-upwind scheme is able to predict
735 the water depths better than s-centered scheme and LISFLOOD-FP. In terms of time to peak flood,
736 all the inertial schemes show certain amount of delay (Table 7), among which the s-upwind scheme
737 has lesser delay followed by the s-centered scheme and LISFLOOD-FP model. The delay might
738 be due to the fact that the advection term is neglected in the momentum equation. Overall, it can

19

739  be concluded that the adaptive $\theta$ concept for local-inertial model is seen to improve the prediction
740  of time-series of water depth in comparison to the LISFLOOD-FP model.

741  ***Comparison of flood extent***

742  The maximum flood extent obtained by HEC-RAS is used as reference solution due to lack of
743  observed inundation extent. For qualitative comparison, actual, under and over predicted areas are
744  shown in three different colours in Figure 22. Figures 22a and 22b imply that the s-upwind and s-
745  cenetered schemes predict inundation extent better than LISFLOOD-FP model (Figure 22c).
746  Quantitative comparisons using the measure of fit function, $F$ (equation 17) emphasize the same
747  conclusion with the values of 94%, 90% and 86% for the proposed s-upwind and s-centered
748  schemes and LISFLOOD-FP, respectively. The contour maps of maximum flood extent are plotted
749  in Figure 23. The difference of maximum flood depth of HEC-RAS with s-schemes and
750  LISFLOOD-FP is within ~ 0.5 m. Altogether the results imply that the local-inertial models can
751  simulate a severe flood event with a level of accuracy similar to that of a full 2D model.

752  The relative computation time of the LISFLOOD-FP model is ~1.32 and ~1.37 times more than
753  that of the proposed s-upwind and s-centered schemes, respectively, whereas, HEC-RAS 2D model
754  takes ~26 times more computation time. Hence, it is clear that the proposed local-inertial model
755  takes significantly less computation time compared to HEC-RAS 2D model. In addition, the
756  proposed s-schemes improve the overall computation time by at least ~1.3 times compared to
757  LISFLOOD-FP model. The computation time of inertial models can be reduced significantly
758  through the implementation of parallel processing as described in the introduction.

759  **6 Conclusions**

760  This study focuses on the development of a rapid flood prediction model with minimum process
761  representation. One such model developed by Bates et al. (2010) and improved by de Almeida et
762  al. (2012) is used in many applications for large-scale flood simulations. For oscillation free
763  solutions, de Almeida et al. (2012) introduced an artificial diffusion term through a weighting
764  factor $\theta$ in the numerical schemes (termed as q-schemes). The value of $\theta$ controls the amount of
765  diffusion and hence determines the flux diffusion through the cell boundaries. As a consequence,
766  the accuracy of the q-schemes depends on the value of $\theta$, which is considered to be an arbitrary
767  constant value and requires repeated trials to arrive at its optimal value. To circumvent this
768  problem, an explicit expression for $\theta$ is proposed in this study, where $\theta$ varies both spatially and
769  temporally, being a function of velocity, water depth, grid and time step size. The proposed
770  adaptive $\theta$ is implemented in the q-schemes proposed in de Almeida et al. (2012) and are termed
771  as s-schemes in this study. The s-schemes are rigorously investigated by simulating the following
772  test cases: (a) nonbreaking wave propagation over a horizontal plane, (b) nonbreaking wave
773  propagation on a planar beach, (c) an experimental 2D steady flow in a river-network-floodplain
774  setup, (d) an urban flood event in Glasgow, UK and (f) Chennai flood of 2015, India.

775  The analytical test cases indicate that the proposed s-schemes perform consistently better than q-
776  schemes for different Manning's $n$ values without numerical oscillations. Further, it is found that
777  the accuracy of upwind scheme is influenced more by the value of weighting factor $\theta$ rather than
778  the zero-th order term associated with the upwind scheme as reported in de Almeida et al. (2012).
779  The simulation of the experimental set-up at IITM demonstrates that the usage of the same constant
780  $\theta$ along both the *x*- and *y*-directions deteriorates the accuracies of predicted inundation extent and

20

781 inappropriate value of $\theta$ can produce nonphysical inundation extent. The proposed s-schemes
782 predict the inundation extent accurately as it maintains the spatial and temporal variations of
783 diffusion value using adaptive $\theta$. The results from the simulation of the urban flood event in
784 Glasgow, UK indicates that the q-schemes still sufferer from numerical instability despite the use
785 of constant $\theta$ value, while the proposed s-scheme delivers smooth solutions for all considered
786 combinations of low frictions. Finally, the large-scale simulation of the disastrous Chennai flood
787 (2015) prove that the proposed s-schemes can simulate a severe flood event with accuracy similar
788 to that of a full 2D model. Overall, the prosed s-schemes improve the model stability and accuracy.

789 The proposed s-schemes are also shown to be stable even at higher value of CFL = 0.9 compared
790 to CFL = 0.8 used in LISFLOOD-FP. As a result, the proposed s-schemes not only improve the
791 numerical stability but also enhances the computational efficiency. Again, q- as well as s-schemes
792 are found to be significantly faster than the HEC-RAS 2D model (~ 25 times). The validation and
793 application prove that the developed local-inertial model with adaptive $\theta$ has the potential to be
794 used in a rapid flood prediction system.

795 The following specific conclusions are drawn from this study.

796     i)   A mathematical expression for adaptive $\theta$ is derived on the basis of water depth, velocity,
797           grid and time step size. This explicit expression eliminates the trial and error procedure
798           used so far in local-inertial models and also solves the problem on numerical instability.
799           The expression can be used in both centered and upwind schemes of local-inertial models,
800           which can be used for rapid large-scale flood prediction.
801     ii)  The rigorous validation and application clearly show that the developed s-schemes with
802           adaptive $\theta$ improve the accuracy when compared to LISFLOOD-FP model for slow rising
803           floods.
804     iii) The adaptive $\theta$ is shown to allow the use of higher CFL value and hence overall
805           computation time is reduced compared to LISFLOOD-FP and 2D models.
806     iv) The proposed adaptive $\theta$ in the s-upwind scheme performs with almost the same accuracy
807           and computation time as that of the s-centered scheme. Hence, the conclusion of de
808           Almeida et al. (2012) that the performance of the upwind scheme is inconsistent is proven
809           to be invalid.
810

815

816

817

818

819

21

820

821

**References**

823 Aricò, C., Filianoti, P., Sinagra, M., & Tucciarelli, T. (2016). The FLO Diffusive 1D-2D Model
824      for Simulation of River Flooding. *Water*, *8*(5), 200. https://doi.org/10.3390/w8050200.

825 Aronica, G., Bates, P. D. Ł., & Horritt, M. S. (2002). Assessing the uncertainty in distributed model
826      predictions. *Hydrological Processes*, 2001–2016. https://doi.org/10.1002/hyp.398

827 Aronica, G., Tucciarelli, T., & Nasello, C. (1998). 2D Multilevel Model for Flood Wave
828      Propagation in Flood-Affected Areas. *Journal of Water Resources Planning and*
829      *Management*,      *124*(4),      210–217.      https://doi.org/10.1061/(ASCE)0733-
830      9496(1998)124:4(210).

831 Bates, P. D., & De Roo, A. P. J. (2000). A simple raster-based model for flood inundation
832      simulation. *Journal of Hydrology*, *236*(1–2), 54–77. https://doi.org/10.1016/S0022-
833      1694(00)00278-X.

834 Bates, P. D., Wilson, M. D., Horritt, M. S., Mason, D. C., Holden, N., & Currie, A. (2006). Reach
835      scale floodplain inundation dynamics observed using airborne synthetic aperture radar
836      imagery :      *Data      analysis      and      modelling*,      306–318.
837      https://doi.org/10.1016/j.jhydrol.2005.12.028.

838 Bates, P. D., Horritt, M. S., & Fewtrell, T. J. (2010). A simple inertial formulation of the shallow
839      water equations for efficient two-dimensional flood inundation modelling. *Journal of*
840      *Hydrology*, *387*(1–2), 33–45. https://doi.org/10.1016/j.jhydrol.2010.03.027.

841 Baugh, C. A., Bates, P. D., Schumann, G., & Trigg, M. A. (2013). SRTM vegetation removal and
842      hydrodynamic modeling accuracy. *Water Resources Research*, *49*(9), 5276–5289.
843      https://doi.org/10.1002/wrcr.20412.

844 Bermudez, A., Rodriguez, C., & Vilar, M. A. (1991). Solving Shallow Water Equations by a Mixed
845      Implicit Finite Element Method. *IMA Journal of Numerical Analysis*, *11*(September 2014),
846      79–97. https://doi.org/10.1093/imanum/11.1.79.

847 Bradbrook, K. F., Lane, S. N., Waller, S. G., & Bates, P. D. (2004). Two dimensional diffusion
848      wave modelling of flood inundation using a simplified channel representation. *International*
849      *Journal of River Basin Management*, *2*(3), 211-223.

850 Brown, J. D., Spencer, T., & Moeller, I. (2007). Modeling storm surge flooding of an urban area
851      with particular reference to modeling uncertainties: A case study of Canvey Island, United
852      Kingdom. *Water Resources Research*, *43*(6), 1–22.https://doi.org/10.1029/2005WR00 4597.

853 Brunner, G.W. (2016). HEC-RAS River Analysis System, Hydraulic Reference Manual (Version
854      5), US Army Corps of Engineers, Davis (2016).

855 Bruwier, M., Archambeau, P., Erpicum, S., Pirotton, M., & Dewals, B. (2017). Shallow-water
856      models with anisotropic porosity and merging for flood modelling on Cartesian grids. *Journal*
857      *of hydrology*, *554*, 693-709.

Cea, L & Blade, E. (2015). A simple and efficient unstructured finite volume scheme for solving the shallow water equations in overland flow applications. *Water Resources Research*, 5464–5486. https://doi.org/10.1002/2014WR016547.

Coulthard, T. J., Neal, J. C., Bates, P. D., Ramirez, J., de Almeida, G. A. M., and Hancock, G. R.: Integrating the LISFLOOD-FP 2D hydrodynamic model with the CAESAR model: implications for modelling landscape evolution, *Earth Surf. Proc. Landf.*, 38, 1897–1906, doi:10.1002/esp.3478, 2013.

de Almeida, G. A. M., Bates, P., Freer, J. E., & Souvignet, M. (2012). Improving the stability of a simple formulation of the shallow water equations for 2-D flood modeling. *Water Resources Research*, *48*(5), 1–14. https://doi.org/10.1029/2011WR011570.

de Almeida, G.A.M. & Bates, P.D. (2013). Applicability of the local-inertial approximation of the shallow water equations to flood modelling. Water Resources Research, 49 (8), 4833–4844. (10.1002/wrcr.20366).

de Paiva, R. C. D., Buarque, D. C., Collischonn, W., Bonnet, M. P., Frappart, F., Calmant, S., & Bulhões Mendes, C. A. (2013). Large-scale hydrologic and hydrodynamic modeling of the Amazon River basin. *Water Resources Research*, *49*(3), 1226–1243. https://doi.org/10.1002/wrcr.20067.

Dottori, F., & Todini, E. (2010). A 2D flood inundation model based on cellular automata approach. In *XVIII International Conference on Water Resources CMWR*. Barcelona.

Falconer, R. A. (1986). Water quality simulation study of a natural harbor. *Journal of Waterway, Port, Coastal, and Ocean Engineering*, *112*(1), 15-34.

Fewtrell, T. J., J. C. Neal, P. D. Bates, & P. J. Harrison, (2011). Geometric and structural river channel complexity and the prediction of urban inundation. *Hydrological Processes*, 25, 3173–3186.

Fewtrell, T., Bates, P.D., Horritt, M., & Hunter, N. (2008). Evaluating the effect of scale in flood inundation modelling in urban environments. *Hydrological Processes*, 22, 5107–5118. (10.1002/hyp.7148).

Guidolin, M., Chen, A. S., Ghimire, B., Keedwell, E. C., Djordjević, S., & Savić, D. A. (2016). A weighted cellular automata 2D inundation model for rapid flood analysis. *Environmental Modelling & Software*, *84*, 378-394.

Hervouet, J.M. (2000). TELEMAC modelling system: An overview. *Hydrological Process*. 14 pp. 2209-2210, 10.1002/1099-1085(200009)14:13<2209:AID-HYP23>3.0.CO;2-6.

Horritt, M. S., & Bates, P. D. (2001). Effects of spatial resolution on a raster based model of Flood flow, *Journal of Hydrology*, *253, 239-249*.

Horritt, M., Bates, P., Fewtrell, T., Mason, D., & Wilson, M. (2010). Modelling the hydraulics of the Carlisle 2005 flood event. *Proceedings of the Institution of Civil Engineers, Water Management*, 163 (6), 273-281. (10.1680/wama.2010.163.6.273).

Hubbard, M. E. (1999). Multidimensional slope limiters for MUSCL-Type of Finite volume schemes on unstructured grids. *Journal of Computational Physics*, *155*, 54–74. https://doi.org/10.1006/jcph.1999.6329.

Hunter, N. M., Bates, P. D., Neelz, S., Pender, G., Villanueva, I., & Wright, N. G. (2008). Benchmarking 2D hydraulic models for urban flooding. *Proceedings of the Institution of Civil Engineers - Water Management*, *161*(1), 13–30. https://doi.org/10.1680/wama.2008.161.1.13.

Hunter, N. M., Horritt, M. S., Bates, P. D., Wilson, M. D., & Werner, M. G. F. (2005). An adaptive time step solution for raster-based storage cell modelling of floodplain inundation. *Advances in Water Resources*, *28*(9), 975–991. https://doi.org/10.1016/j.advwatres.2005.03.007

Kalyanapu, A. J., Shankar, S., Pardyjak, E. R., Judi, D. R., & Burian, S. J. (2011). Environmental Modelling & Software Assessment of GPU computational enhancement to a 2D fl ood model. *Environmental Modelling and Software*, 26(8), 1009–1016. https://doi.org/10.1016/j.envsoft.2011.02.014.

Kuiry, S. N., Ding, Y., & Wang, S. S. Y. (2010). Modelling coastal barrier breaching flows with well-balanced shock-capturing technique. *Computers and Fluids*, *39*(10), 2051–2068. https://doi.org/10.1016/j.compfluid.2010.07.015.

Kuiry, S. N., Pramanik, K., & Sen, D. (2008). Finite volume model for shallow water equations with improved treatment of source terms. *Journal of Hydraulic Engineering*, *134*(2), 231-242.

Lamb, R., Crossley, M., & Waller, S. (2009). A fast two-dimensional floodplain inundation model. In *Proceedings of the Institution of Civil Engineers-Water Management* (Vol. 162, No. 6, pp. 363-370). Thomas Telford Ltd.

Lewis, M., Bates, P., Horsburgh, K., & Schumann, G. (2013). A storm surge inundation model of the northern Bay of Bengal using publicly available data A Bay of Bengal Storm Surge Inundation Model, (January), 358–369. https://doi.org/10.1002/qj.2040.

Liang, D., Falconer, R. A., & Lin, B. (2006). Comparison between TVD-MacCormack and ADI-type solvers of the shallow water equations. *Advances in water resources*, *29*(12), 1833-1845.

Liang, Q. (2010). Flood Simulation Using a Well-Balanced Shallow Flow Model, *136*(September), 669–675.

Mali, V. K., & Kuiry, S. N. (2018). Assessing the accuracy of high-resolution topographic data generated using freely available packages based on SfM-MVS approach. *Measurement*, *124*, 338–350. https://doi.org/10.1016/j.measurement.2018.04.043.

Mali, V. K., & Kuiry, S. N. (2019). Experimental and numerical study of flood in a river-network-floodplain set-up. *Journal of Hydraulic Research*, 1-19.

Martins, R., Leandro, J., & Djordjević, S. (2015). A well balanced Roe scheme for the local-inertial equations with an unstructured mesh. *Advances in Water Resources*, *83*, 351–363. https://doi.org/10.1016/j.advwatres.2015.07.007

Narasimhan, B., Bhallamudi, S. M., Mondal, A., Ghosh, S., & Mujumdar, P. (2016). Chennai floods 2015: A rapid assessment. *Bangalore: Interdisciplinary Centre for Water Research, IISc. Retrieved from Http://Itra. Medialabasia. in/Img/Chennai% 20Floods-Rapid% 20Assessment% 20Report-May*, *2023*(May), 202016

Neal, J., Bates, P.D., Fewtrell, T., Hunter, N., Wilson, M., & Horritt, M. (2009). Distributed whole city water level measurements from the Carlisle 2005 urban flood event and comparison with

hydraulic model simulations. *Journal of Hydrology*, 368, 42-55. (10.1016/j.jhydrol.2009.01.026).

Neal, J., Fewtrell, T., & Trigg, M. (2009). Environmental Modelling & Software Parallelisation of storage cell flood models using OpenMP. *Environmental Modelling and Software*, 24(7), 872–877. https://doi.org/10.1016/j.envsoft.2008.12.004

Neal, J., Schumann, G., & Bates, P. (2012). A subgrid channel model for simulating river hydraulics and floodplain inundation over large and data sparse areas. *Water Resources Research*, *48*(11), 1–16. https://doi.org/10.1029/2012WR012514.

Neal, J., Villanueva, I., Wright, N., Willis, T., Fewtrell, T., & Bates, P.D. (2012). How much physical complexity is needed to model flood inundation? *Hydrological Processes*, 26 (15), 2264-2282. (10.1002/hyp.8339).

Néelz, S., & Pender, G. (2013). Benchmarking the latest generation of 2D hydraulic modelling packages. *Environment Agency, Horison House, Deanery Road, Bristol, BS1 9AH*.

Nithila Devi . N., Sridharan, B., & Kuiry, S. N. (2019). Impact of urban sprawl on future fl ooding in Chennai city , India. *Journal of Hydrology*, *574*(April), 486–496. https://doi.org/10.1016/j.jhydrol.2019.04.041.

Pappenberger, F., Beven, K. J., Hunter, N. M., Bates, P. D., Gouweleeuw, B. T., Thielen, J., & de Roo, A. P. J. (2005). Cascading model uncertainty from medium range weather forecasts (10 days) through a rainfall-runoff model to flood inundation predictions within the European Flood Forecasting System (EFFS). *Hydrology and Earth System Sciences*, *9*(4), 381–393. https://doi.org/10.5194/hess-9-381-2005.

Parkes, B. L., Cloke, H. L., Pappenberger, F., Neal, J., & Demeritt, D. (2013). Reducing Inconsistencies in Point Observations of Maximum Flood Inundation Level, *Earth interactions*, *17*(6). https://doi.org/10.1175/2012EI000475.1

Pau, J. C., & Sanders, B. F. (2006). Performance of Parallel Implementations of an Explicit Finite-Volume Shallow-Water Model, *Journal of Computing in Civil Engineering*, 20(2), 99–110.

Peraire, J.,O., C. Zienkiewicz., & Morgan. K. (1986), Shallow water problems: A general explicit formulation, *Int. J. Num. Methods Eng*., 22,547–574.

Ponce, V. M. (1990), Generalized diffusion wave equation with inertial effects, *Water Resources Research*, 26(5), 1099–1101.

Ponce, V. M., R. M. Li., & Simons D. B. (1978), Applicability of kinematic and diffusion models, *Journal of Hydraulic Engineering*, 104, 353–360.

Pontes, P.R.M., Fan, F.M., Fleischmann, A.S., de Paiva, R.C.D., Buarque, D.C., Siqueira, V.A., Jardim, P.F., Sorribas, M.V., & Collischonn, W. (2017). Environmental Modelling & Software MGB-IPH model for hydrological and hydraulic simulation of large fl oodplain river systems coupled with open source GIS, *94*. https://doi.org/10.1016/j.envsoft.2017.03.029.

Sampson, C.C., Fewtrell, T.J., Duncan, A., Shaad, K., Horritt, M.S., & Bates, P.D. (2012). Using terrestrial laser scanning data to drive decimetric resolution urban inundation models. *Advances in Water Resources*, 41, 1-17. (10.1016/j.advwatres.2012.02.010).

Sanders, B. F., Schubert, J. E., & Gallegos, H. A. (2008). Integral formulation of shallow-water

equations with anisotropic porosity for urban flood modeling. *Journal of Hydrology*, *362*(1–2), 19–38. https://doi.org/10.1016/j.jhydrol.2008.08.009.

Sanyal, J., Carbonneau, P., & Densmore, A. L. (2013). Hydraulic routing of extreme floods in a large ungauged river and the estimation of associated uncertainties: A case study of the Damodar River, India. *Natural Hazards*, *66*(2), 1153–1177. https://doi.org/10.1007/s11069-012-0540-7.

Shustikova, I., Domeneghetti, A., Neal, J. C., Bates, P., & Castellarin, A. (2019). Comparing 2D capabilities of HEC-RAS and LISFLOOD-FP on complex topography. *Hydrological Sciences Journal*, *64*(14), 1769-1782.

Seyoum, S. D., Vojinovic, Z., Price, R. K., & Weesakul, S. (2012). Coupled 1D and Noninertia 2D Flood Inundation Model for Simulation of Urban Flooding, *138*(January), 23–34. https://doi.org/10.1061/(ASCE)HY.1943-7900.

Syme, W. J. (1991). Dynamically Linked Two-dimensional/One- dimensional Hydrodynamic Modelling Program for Rivers, Estuaries & Coastal Waters. MEngSc thesis, University of Queensland, Australia.

Toro, E. F. (2001). *Shock-capturing methods for free-surface shallow flows*, Wiley, New York.

Villanueva, I., & Wright, N. G. (2006). Linking Riemann and storage cell models for flood prediction. In *Proceedings of the Institution of Civil Engineers-Water Management* (Vol. 159, No. 1, pp. 27-33). Thomas Telford Ltd.

Xia, R. (1994), Impact of coefficients in momentum equation on selection of inertial models, *Journal of Hydraulic Research*, 32, 615–621.

Yamazaki, D., de Almeida, G. A., & Bates, P. D. (2013). Improving computational efficiency in global river models by implementing the local inertial flow equation and a vector-based river network map. *Water Resources Research*, *49*(11), 7221-7235.

Yan, K., Papenberger, F., Umer, Y. M., Solomatine, D. P., & Baldassarre, G. D. I. (2014). Regional versus physically-based methods for flood inundation modelling in data scarce areas: an application to the Blue Nile. *11th International Conference on Hydroinformatics - HIC 2014*.

Ying, X., Khan, A. A., & Wang, S. S. Y. (2004). Upwind Conservative Scheme for the Saint Venant Equations. *Journal of Hydraulic Engineering*, *130*(10), 977–987. https://doi.org/10.1061/(ASCE)0733-9429(2004)130:10(977).

Yu, D., & Lane, S. N. (2011). Interactions between subgrid-scale resolution, feature representation and grid-scale resolution in flood inundation modelling. *Hydrological Processes*, *25*(1), 36-53.

1018

1019

1020

1021  **Table 1.** Comparison of inundation fitness and computation time of inertial schemes for 0.078
1022  $m^3/s$

| Schemes | Fitness (%) | Relative computation time |
|---------|---------|---------|
| s-upwind | 86 | 1.02 |
| s-centered | 84 | 1.00 |
| LISFLOOD-FP ($\theta = 0.85$) | 66 | 1.19 |
| LISFLOOD-FP ($\theta = 0.90$) | 76 | 1.17 |
| LISFLOOD-FP ($\theta = 0.95$) | 56 | 1.15 |

1023

1024  **Table 2.** RMSE (m) of water surface elevation of s-scheme and LISFLOOD-FP model for 0.078
1025  $m^3/s$

| Schemes | River | Flood plain |
|---------|-------|-------------|
| s-upwind | **0.83** | 0.70 |
| s-centered | 0.98 | 0.76 |
| LISFLOOD-FP ($\theta = 0.85$) | 1.68 | 2.60 |
| LISFLOOD-FP ($\theta = 0.90$) | 1.08 | 0.91 |
| LISFLOOD-FP ($\theta = 0.95$) | 1.23 | 2.52 |

1026

1027  **Table 3.** Comparison of fitness values for inundation extent and computation times of inertial
1028  schemes for 0.098 $m^3/s$

| Schemes | Fitness (%) | Relative computation time |
|---------|---------|---------|
| s-upwind | 92 | 1.03 |
| s-centered | 89 | 1.00 |
| LISFLOOD-FP ($\theta = 0.85$) | 87 | 1.21 |

27

| | | |
|---|---|---|
| LISFLOOD-FP ($\theta = 0.90$) | 82 | 1.18 |
| LISFLOOD-FP ($\theta = 0.95$) | 79 | 1.14 |

1029

1030　**Table 4.** RMSE (m) of water surface elevation of s-scheme and LISFLOOD-FP model for 0.098
1031　$m^3/s$

| Schemes | River | Flood plain |
|---|---|---|
| s-upwind | **0.73** | 0.81 |
| s-centered | 0.72 | 1.02 |
| LISFLOOD-FP ($\theta = 0.85$) | 1.03 | 0.99 |
| LISFLOOD-FP ($\theta = 0.90$) | 0.76 | 1.35 |
| LISFLOOD-FP ($\theta = 0.95$) | 1.22 | 1.82 |

1032

1033　**Table 5**. Friction coefficient values used for the second case

| Simulation No. | $n_{road}$ | $n_{veg}$ |
|---|---|---|
| 1 | 0.008 | 0.015 |
| 2 | 0.009 | 0.020 |
| 3 | 0.010 | 0.025 |
| 4 | 0.011 | 0.030 |
| 5 | 0.012 | 0.035 |
| 6 | 0.013 | 0.040 |
| 7 | 0.014 | 0.045 |
| 8 | 0.015 | 0.050 |
| 9 | 0.016 | 0.055 |
| 10 | 0.017 | 0.060 |
| 11 | 0.018 | 0.065 |
| 12 | 0.019 | 0.070 |
| 13 | 0.020 | 0.075 |

28

1034

1035

1036

1037    **Table 6.** Comparison of errors in peak water depth with respect to HEC-RAS solutions

| Schemes | Error in peak water depth (m) | | | | | |
|---|---|---|---|---|---|---|
| | Gauge 1 | Gauge 2 | Gauge 3 | Gauge 4 | Gauge 5 | Gauge 6 |
| s-upwind | 0.007 | 0.198 | 0.231 | -0.020 | -0.055 | -0.031 |
| s-centered | 0.258 | 0.467 | 0.547 | -0.422 | 0.154 | 0.153 |
| LISFLOOD-FP ( $\theta = 0.8$) | 0.411 | 0.619 | 0.649 | -0.280 | 0.308 | 0.177 |

1038

1039    **Table 7.** Comparison of errors in time to peak flood with respect to HEC-RAS solutions

| Schemes | Error in time to peak flood (min) | | | | | |
|---|---|---|---|---|---|---|
| | Gauge 1 | Gauge 2 | Gauge 3 | Gauge 4 | Gauge 5 | Gauge 6 |
| s-upwind | -27 | -2 | -32 | -16 | -16 | -1 |
| s-centered | -35 | -17 | -35 | -28 | -20 | -8 |
| LISFLOOD-FP ( $\theta = 0.8$) | -40 | -19 | -36 | -34 | -26 | -12 |

1040

1041

1042

1043

1044

1045

1046

1047

1048

1049

1050

1051

29

1052

1053

1054

1055

1056 **Figure Captions**

1057 **Figure 1.** Grid and variables used in the numerical scheme.

1058 **Figure 2.** Diffusion and velocity profile obtained by the proposed s-schemes at $t$ = 2700, 5400,
1059 and 9000 s for (e) 0.01 and (f) 0.005 m$^{-1/3}$s.

1060 **Figure 3.** Predicted water surface elevation at $t$ = 1080, 2160, 2800 and 3600 s using a uniform
1061 Manning coefficient of (a) 0.03 and (b) 0.01 m$^{-1/3}$s; (c) and (d) are the zoomed-in view of (a) and
1062 (b) at $t$ = 3600 s.

1063 **Figure 4.** IITM physical model setup showing the observation locations in the river and over the
1064 floodplain.

1065 **Figure 5**. Comparison of simulated and observed inundation extent maps for LISFLOOD with $\theta$
1066 = (a) 0.85, (b) 0.90, (c) 0.95, (d) s-centered scheme and (e) s-upwind scheme for the steady-state
1067 discharge of 0.078 m$^3$/s.

1068 **Figure 6.** Diffusion and velocity dependence for s-upwind scheme: along $x$-direction (a) diffusion,
1069 (b) velocity and along $y$-direction (c) diffusion and (d) velocity. Diffusion and velocity dependence
1070 for s-centered scheme: along $x$-direction (a) diffusion, (b) velocity and along $y$-direction (c)
1071 diffusion and (d) velocity.

1072 **Figure 7**. Comparison of simulated and observed water depths in the river branches.

1073 **Figure 8**. Comparison of simulated and observed water depth over floodplains

1074 **Figure 9**. Comparison of simulated and observed inundation extent maps for LISFLOOD with (a)
1075 $\theta$ =0.85, (b) $\theta$ =0.90, (c) 0.95, (d) s-centered scheme and (e) s-upwind scheme for the steady-state
1076 discharge of 0.098 m$^3$/s.

1077 **Figure 10.** Diffusion and velocity dependence for s-upwind scheme: along $x$-direction (a)
1078 diffusion, (b) velocity and along $y$-direction (c) diffusion and (d) velocity.

1079 **Figure 11**. Comparison of simulated and observed water depths in the river branches.

1080 **Figure 12**. Comparison of simulated and observed water depth over floodplains

1081 **Figure 13.** The Greenfield study site in Glasgow, UK (a) building and road network and (b) aerial
1082 photograph.

1083 **Figure 14**. Comparison of water depths at stations (a) X1 (b) X2, (c) X3 and X4.

1084 **Figure 15**. Comparison of inundation extents predicted by (a) s-upwind, (b) s-centered scheme
1085 with (c) full 2D model available in LISFLOOD-FP suite.

30

1086     **Figure 16.** Water depth time series simulated using LISFLOOD-FP inertial model at (a) X1 (b)
1087     X2, (c) X3 and X4 for simulation no 1, 7 and 13 in Table 5.

1088     **Figure 17.** Water depth time series simulated using s-upwind scheme at (a) X1 (b) X2, (c) X3 and
1089     X4 for the ensample of Manning's roughness coefficients provided in Table 5.

1090     **Figure 18.** Water depth time series simulated using s-centered scheme at (a) X1 (b) X2, (c) X3
1091     and X4 for the ensample of Manning's roughness coefficients provided in Table 5.

1092     **Figure 19.** Map of the study area, Adyar basin. The red dot and the pink line indicate the location
1093     where the upstream and downstream boundary conditions, respectively are specified. Green dots
1094     indicate the locations where the time-series of water depth are compared.

1095     **Figure 20.** Scatter plot of simulated vs. observed maximum flood depths for 2015 flood in Chennai
1096     city.

1097     **Figure 21:** Comparison of time-series of water depth at (a) Gauge 1, (b) Gauge 2, (c) Gauge 3, (d)
1098     Gauge 4, (e) Gauge 5 and (f) Gauge 6.

1099     **Figure 22:** The maximum flood extent predicted by (a) s-upwind, (b) s-centered and (c)
1100     LISFLOOD-FP.

1101     **Figure 23:** The maximum flood extent predicted by (a) HEC-RAS, (b) s-upwind, (c) s-centered
1102     and (d) LISFLOOD-FP.

1103

1104

1105

1106

1107

1108

1109

31

(a)

(b)

(c)

(d)

(e)

(f)

(g)

(h)

Analytical

s-centered                          s-upwind

q-centered ($\theta = 0.8$)          q-centered ($\theta = 0.9$)

q-upwind ($\theta = 0.8$)            q-upwind ($\theta = 0.9$)

(a)                                    (b)

(c)                                    (d)

Runge-Kutta

........ s-centered              ——— s-upwind

—·—· q-centered (θ = 0.8)        —·—· q-centered (θ = 0.9)

——— q-upwind (θ = 0.8)          ——— q-upwind (θ = 0.9)

F1 – F5: Floodplain

(a)



(b)



(c)



(d)



(e)

(a)　　　　　　　　　　　　　　　　(b)

(c)　　　　　　　　　　　　　　　　(d)

(e)　　　　　　　　　　　　　　　　(f)

(g)　　　　　　　　　　　　　　　　(h)

0.02 0.04 0.06 0.08 0.1 0.12 0.14 0.16 0.18 0.2 0.22 0.24

-1.00 -0.75 -0.50 -0.25 0.00 0.25 0.50 0.75 1.00

Legend:
■ Observed   ★ s-upwind   ○ s-centered
▲ LISFLOOD-FP (θ=0.85)   ● LISFLOOD-FP (θ=0.90)   ▲ LISFLOOD-FP (θ=0.95)

X-axis: River gauge
Y-axis: Water depth (cm)

(a)



(b)



(c)



(d)



(e)

(a)

(b)

(c)

(d)

(e)

(f)

(g)

(h)

0.02 0.04 0.06 0.08 0.1 0.12 0.14 0.16 0.18 0.2 0.22 0.24

-1.00 -0.75 -0.50 -0.25 0.00 0.25 0.50 0.75 1.00

(a)



(b)

(a)

(b)

(c)

(d)

········ s-centered     —— s-upwind     ------ JFLOW     —— TRENT
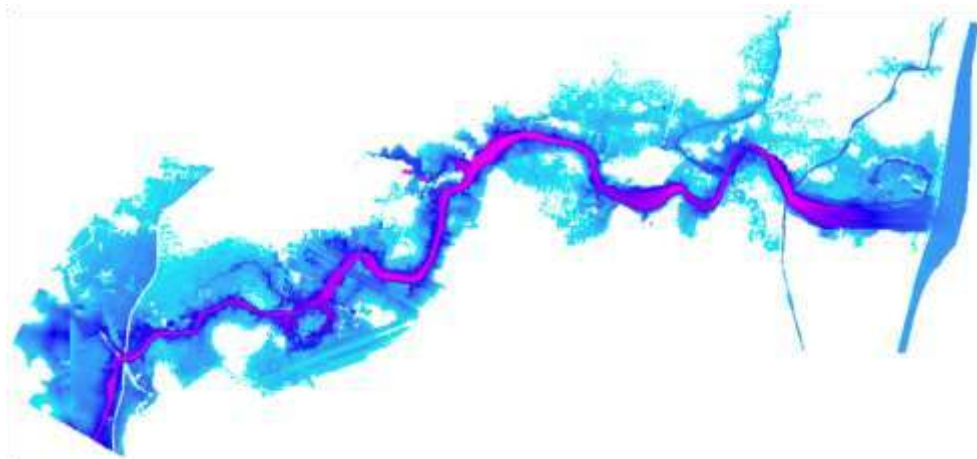
—— D-TVD     —— DIVAST     —— TUFLOW

—— LISFLOOD-FP (DIFFUSIVE)     —— LISFLOOD-FP (INERTIAL)

(a)



(b)



(c)

Water depth (m)

0.1 0.2 0.3 0.4 0.5 0.6 0.7 0.8

(a)                      (b)

(c)                      (d)

LISFLOOD-FP (Sim. No. 1)       LISFLOOD-FP (Sim. No. 7)

LISFLOOD-FP (Sim. No. 13)       Full 2D model (min & max)

(a)

(b)

(c)

(d)

Ensemble of s-upwind    s-upwind (min & max)

Full 2D model (min & max)

Ensemble of s-centered ——— s-centered (min & max)

Full 2D model (min & max)

(a)

(b)

(c)

(d)

(e)                                                    (f)

- - - - -   s-centered   ———— s-upwind   —·—·—· LISFLOOD-FP (θ = 0.8)
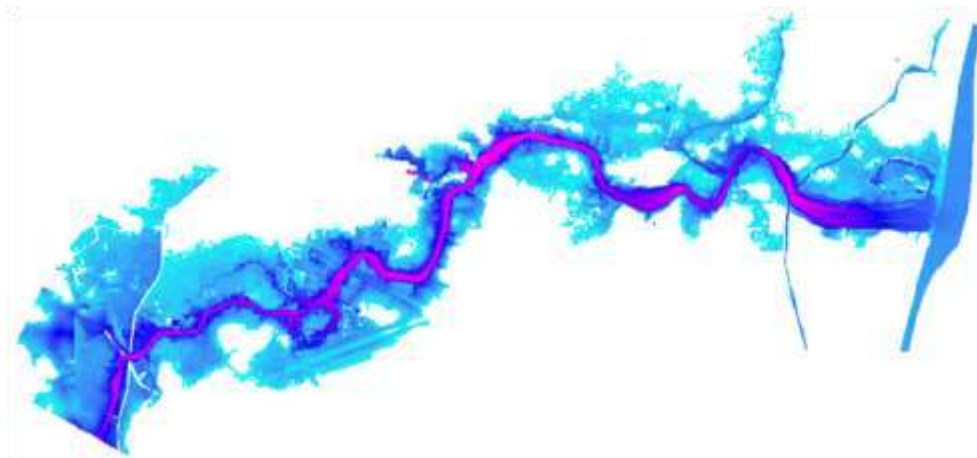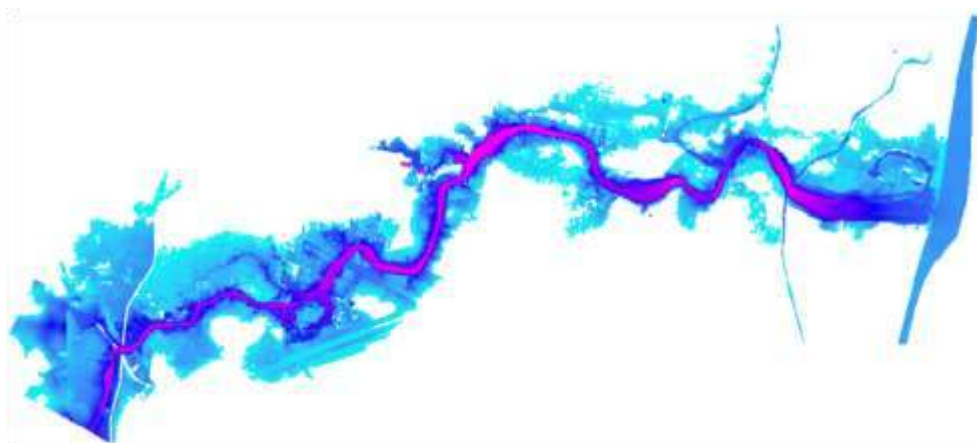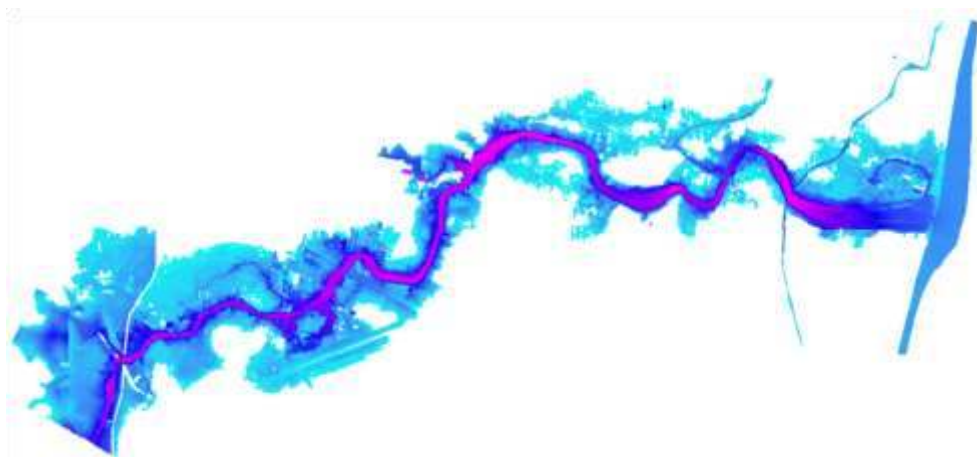
———— HEC-RAS   - - - - - - TELEMAC2D

(a)



(b)



(c)

(a)



(b)



(c)

(d)

Water depth (m)

12.70                    0